DIGITAL ACCESS TO SCHOLARSHIP AT HARVARD
DASH.HARVARD.EDU

HARVARD LIBRARY
Office for Scholarly Communication

When the Circadian Clock Cannot Be Set: An Unstable Singularity Underlies Stochastic Phasing of the Circadian Clock in Individual Cyanobacterial Cells

Permanent link
http://nrs.harvard.edu/urn-3:HUL.InstRepos:39945333

Terms of Use
This article was downloaded from Harvard University's DASH repository, and is made available under the terms and conditions applicable to Other Posted Material, as set forth at http://nrs.harvard.edu/urn-3:HUL.InstRepos:dash.current.terms-of-use#LAA

Share Your Story

The Harvard community has made this article openly available.
Please share how this access benefits you. Submit a story .

Accessibility

When the circadian clock cannot be set: An unstable singularity underlies stochastic phasing of the circadian clock in individual cyanobacterial cells

A dissertation presented

by

Siting Gan

to

The Committee on Higher Degrees in Systems Biology

in partial fulfillment of the requirements

for the degree of

Doctor of Philosophy

in the subject of

Systems Biology

Harvard University

Cambridge, Massachusetts

November 2017

© 2017 – Siting Gan

All rights reserved.

Advisor: Professor Erin K. O'Shea **Author: Siting Gan**

When the circadian clock cannot be set: An unstable singularity underlies stochastic phasing of the circadian clock in individual cyanobacterial cells

Abstract

The endogenous circadian clock synchronizes with environmental time by appropriately resetting its phase in response to external cues. Of note, some resetting stimuli induce attenuated oscillations of clock output, which has been observed at the population-level in several organisms and in studies of individual humans. To investigate what is happening in individual cellular clocks, we studied the unicellular cyanobacterium *S. elongatus*. By measuring its phase resetting responses to temperature changes, we found that population-level arrhythmicity occurs when certain perturbations cause stochastic phases of oscillations in individual cells. Combining modeling with experiments, we related stochastic phasing to the dynamical structure of the cyanobacterial clock as an oscillator, and explored the physiological relevance of the oscillator structure for accurately-timed rhythmicity in changing environmental conditions. Our findings and approach can be applied to other biological oscillators.

Table of Contents

List of figures

List of tables

Acknowledgements

Graduate school has been a truly inspiring and rewarding experience for me. First and foremost, I would like to thank my advisor Prof. Erin O'Shea and the entire O'Shea lab. After graduating from college as a physics major, I started the Ph.D. program with little appreciation of biology as an experimental science – I used to imagine that findings could be derived and experimental conditions tuned at wish. Throughout years of training with Erin, I learned to formulate clear and interesting research questions, to rigorously design and execute experiments, and to apply quantitative analysis and modeling in an illuminating fashion. I also owe much of my improvement in scientific communication to Erin's timely and constructive feedback. Moreover, closely viewing Erin who started out as a biochemist and has worked on many different problems before lately switching to neuroscience, I picked up some of her fearlessness in tackling new scientific questions and learning whatever is needed to do so. Such learning experience was also supported and inspired by my labmates, who came from various backgrounds and each took on projects involving initially unfamiliar technologies or disciplines. I am grateful for their camaraderie and for making the O'Shea lab a stimulating place to do science.

I would also like to thank Prof. Andrew Murray, Prof. Charles Weitz, Prof. Michael Springer, Prof. Elizabeth Klerman, and Prof. Timothy Mitchison for generously taking time from their busy schedules to serve on my DAC and/or dissertation committees, and for helping me identify the areas where I need to keep pushing forward, in terms of both developing the research project and growing as a scientist in general. I am also grateful for my HGWISE (Harvard Graduate Women in Science and Enginering) mentor Prof. Emily Balskus for the many inspiring and open-hearted

discussions throughout the years. I wanted to thank Peter Arvidson and Jeffrey Offermann for their dedication to making everything much easier in the O'Shea lab, and Samantha Reed and Elizabeth Pomerantz for bringing joy and warmth to the community of Systems Biology, and for cheering us students along throughout the somewhat strenuous Ph.D. journey. I was also extremely fortunate to share this journey with my Systems Biology classmates and many good friends and colleagues in the Northwest building.

Last but not the least, I would like to express my deepest gratitude for my mother Huijin Li and father Peizhong Gan for their unconditional love. I stayed close to home during college, so coming to the U.S. for graduate school felt like a sudden separation for my parents. They were nevertheless always understanding and supportive of me. I would finally like to close the acknowledgements with my husband Yuyin Allen Chen, a fellow scientist with high standards for clear thinking and communication. During the many days when my research project did not seem to be going anywhere, the fact that discussing with him about it resulted in less and less intense an argument has served as a tangible marker for my slow progress, encouraging me along the way.

Contributions

S.G. and E.K.O. designed research. S.G. performed research. S.G. and E.K.O. wrote the manuscript, which has previously been published as the following paper:

Gan, S., and O'Shea, E.K. (2017). An Unstable Singularity Underlies Stochastic Phasing of the Circadian Clock in Individual Cyanobacterial Cells. Mol. Cell *67*, 659–672.e12.

This work was supported by the Howard Hughes Medical Institute.

Chapter 1

Introduction

The circadian clock (Dunlap et al., 2009) generates an internal representation of the time that enables an organism to anticipate daily changes in the environment and adapt its physiology. The clock can be entrained and synchronized with external diurnal (daily) cycles, which is achieved by resetting the phase of the clock in response to cues such as temperature or light/darkness (Fig. 1A, blue line to red line). Of special interest, certain resetting stimuli trigger a loss of robust circadian rhythms (i.e. zero amplitude; Fig. 1B, blue line to red line). First observed in the 1970s, this

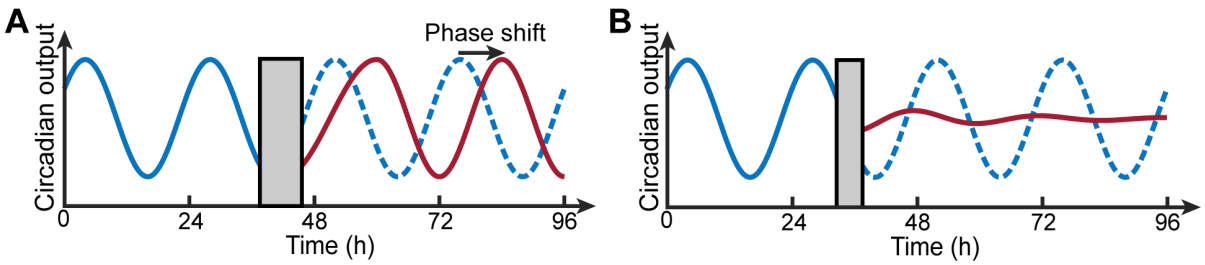

Figure 1. Schematics of phase resetting responses – **(A)** typical phase shift and **(B)** induced loss of oscillations at a population level. The solid blue and red lines respectively represent dynamics of a clock output before and after a resetting signal (gray bar). The dashed blue line is extended from the solid blue line to assist the comparison of pre- and post-signal dynamics.

phenomenon has been reported in many circadian systems by measuring population-averaged overt rhythms of physiology that are regulated by the clock (Engelmann et al., 1978; Grone et al., 2011; Huang et al., 2006; Johnson and Kondo, 1992; Malinowski et al., 1985; Peterson, 1980; Saunders, 1978; Taylor et al., 1982; Winfree, 1970, 2010). The resetting-stimuli-induced interruption of robust rhythms has also been observed in other biological oscillators with periods that span a broad range of timescales, such as cardiac pacemaker cells (Meerwijk et al., 1984) and

the neural respiratory system (Paydarfar et al., 1986). Since circadian oscillations exist in individual cells (Bell-Pedersen et al., 2005; Deng et al., 2016; Mihalcescu et al., 2004; Nagoshi et al., 2004; Plautz et al., 1997; Yakir et al., 2011), attenuated oscillations of organismal clock output at the population level can thus be attributed to either suppression of circadian rhythms in individual cellular clocks or loss of synchrony among a population of initially synchronized clocks (Fig. 2; top vs. bottom) (Leloup and Goldbeter, 2000; Ukai et al., 2007). To distinguish between

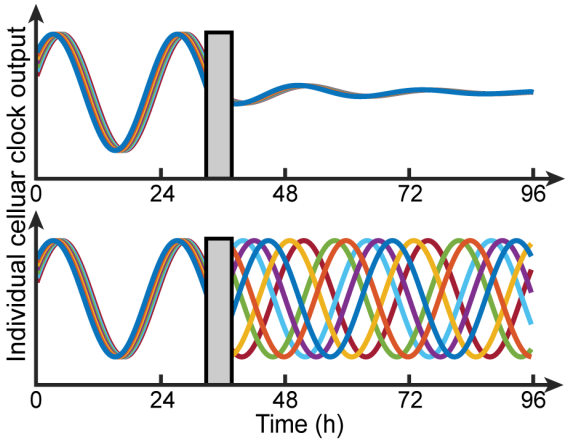

Figure 2. Two models for the single-cell behavior underlying the phenomenon illustrated in Fig. 1B – arrhythmicity (top) vs. loss of synchrony (bottom) among individual cellular clocks, whose dynamics are represented by colored traces.

these two possibilities, two recent studies (Pulivarthy et al., 2007; Ukai et al., 2007) synthetically produced light responsiveness in cell culture systems with the mammalian cellular clock, but reached somewhat different conclusions regarding whether it is desynchronization alone (Ukai et al., 2007) or a combination of both desynchronization and suppression of cellular rhythms (Pulivarthy et al., 2007) that underlies the attenuated population-level oscillations in response to a critical light pulse. To further resolve the cellular behavior in an intact organismal clock, we studied the model system of the unicellular cyanobacterium *S. elongatus* PCC 7942, whose state

can be directly measured at the single-cell level (Chabot et al., 2007; Mihalcescu et al., 2004; Teng et al., 2013; Yang et al., 2010).

The cyanobacterial circadian clock is well characterized and consists of three proteins (KaiA, KaiB, KaiC) that generate oscillations in the phosphorylation state of KaiC (Nishiwaki et al., 2007; Rust et al., 2007), which controls the activity of RpaA (Markson et al., 2013; Takai et al., 2006; Taniguchi et al., 2010). RpaA is the master transcription factor (Markson et al., 2013) that drives circadian gene expression, including circadian expression of genes encoding two clock components, *kaiBC* (Fig. 3). To monitor phase resetting responses, we expressed a fluorescent protein (YFP) under the control of the *kaiBC* promoter (Chabot et al., 2007; Teng et al., 2013; Yang et al., 2010), allowing us to continuously track the state of individual cellular clocks by live cell imaging (Fig. 3). We chose a low-temperature pulse, specifically a 25°C pulse in a 35°C

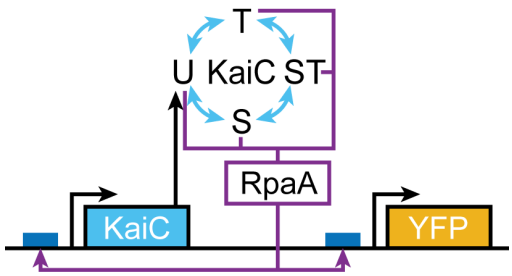

Figure 3. Diagram of the genetic circuits of the cyanobacterial circadian clock and the transcriptional reporter of clock state. KaiC has two phosphorylation sites and transits through four phosphorylated forms during the circadian cycle – unphosphorylated (U-KaiC, represented by 'U'); phosphorylated only on T432 (T-KaiC, 'T'); phosphorylated on both S431 and T432 (ST-KaiC, 'ST'); and phosphorylated only on S431 (S-KaiC, 'S'). This cycling of KaiC phosphorylation state drives oscillations in the level of phosphorylated RpaA (Rpa~P), which directly regulates the transcriptional activity of the *kaiBC* promoter, and thereby the expression of KaiC. The clock-state reporter is built by expressing a fluorescent protein – YFP fusion under the control of the *kaiBC* promoter.

background, as a type of resetting signal that might induce attenuated oscillations at the population level. These conditions were selected to encompass a wide enough range of temperature to induce changes in the clock but still be within the range of normal clock function and cell growth (Kondo et al., 1993). We did not choose the most frequently used signal of a dark pulse in constant light because although the core clock keeps oscillating in the dark, the YFP reporter cannot track its state due to global inhibition of transcription that occurs in darkness (Ito et al., 2009). We identified low-temperature pulses that trigger desynchronization of a population of initially synchronized cells. By systematically measuring phase resetting responses and analyzing experimental data with limit cycle theory and modeling, we unraveled the mechanisms underlying stochastic phasing and loss of population-level oscillations. The mechanisms can be generalized beyond the signals devised for this study, and possibly applied to other biological oscillators.

Chapter 2

Results

2.1 Multiple critical perturbations induce stochastic phases, resulting in population-averaged attenuation of oscillations

To identify the critical 25°C-pulse perturbations that cause attenuation of oscillations at the population-averaged level, we scanned the phase resetting responses to a 25°C pulse by varying the pulse duration (τ) from 0 to 24 h with a 3 h step (Fig. 4, left), and the initial circadian phase (φ_{ini}) at the time the pulse was given from 0° to 360° (Fig. 4, right). In response to a resetting

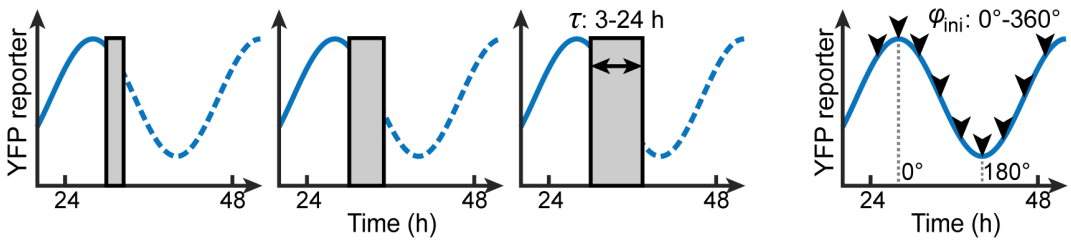

Figure 4. Two systematically scanned variables – the 25°C pulse duration (τ, left three panels, exemplified by three different widths of gray bars) and the initial phase at which the pulse is given (φ_{ini}, right panel, represented by black arrows).

stimulus, the circadian clock will gradually modulate its trajectory. Thus, following a 25°C pulse, it takes a period of transient dynamics (Fig. 5, orange line) to establish a stable (termed 'steady-state') phase shift. To quantify the steady-state resetting responses, we traced the new stabilized rhythms (Fig. 5, red line) backward to infer what the phase of the clock would be when the 25°C pulse was given, and then denote the new phase (φ_{ini}) by this extrapolated clock state at the onset of the pulse (Fig. 5, red arrow) (see Methods for the imaging protocol and analysis).

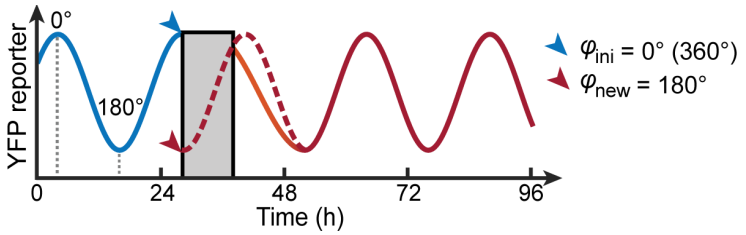

Figure 5. Schematic explaining how to quantify the phase shift (blue line to red line) in response to a 25°C pulse. The orange line denotes the transient dynamics it takes the clock to establish stabilized rhythms after the pulse (red line), while the dashed red line demonstrates tracing the stabilized rhythms back to the onset of the pulse. With 0° set to the peak of a cosine fit (and 180° to the trough), in this example plot, the 25°C pulse applied at $\varphi_{\mathrm{ini}} = 0°$ (highlighted by blue arrow) resets the clock to $\varphi_{\mathrm{new}} = 180°$ (red arrow).

By scanning the phase resetting responses, we found multiple critical perturbations that induce stochastic phases following a 25°C pulse, and thereby cause attenuation of circadian oscillations at the population-averaged level. A perturbation refers to a certain length of 25°C pulse applied at a particular initial phase – a unique combination of the two scanned variables (τ, φ_{ini}). For example, when a 12 h shift to 25°C is applied at φ_{ini}~186°, it triggers stochastic cellular responses – initially synchronized cells descended from the same mother cell become desynchronized after the pulse (Fig. 6A, top). Notably, when the same 12 h shift to 25°C is applied at other circadian phases, for example φ_{ini}~75°, we observed deterministic phase resetting responses (Fig. 6A, bottom). The responses to a 12 h shift to 25°C can be summarized by plotting the new phase (φ_{new}) as a function of the initial phase (φ_{ini}) (Fig. 6B). For cells with an average $\varphi_{\mathrm{ini}} = 75°$ at the time the pulse was given, the new phases are tightly distributed (Fig. 6B, red points), which indicates a one-to-one mapping from the initial phase to the new phase. For the cells with an average $\varphi_{\mathrm{ini}} = 186°$, the ~360° scattering of φ_{new} implies that the new phase is stochastic and unpredictable (Fig. 6B, light blue points). The single-cell responses to a 12 h pulse given at different values of φ_{ini} ranging from 0° to 360° can be summarized with a single-cell phase transition curve (PTC) (Johnson, 1999), which demonstrates stochastic responses as a divergence in φ_{new} at φ_{ini}~186°

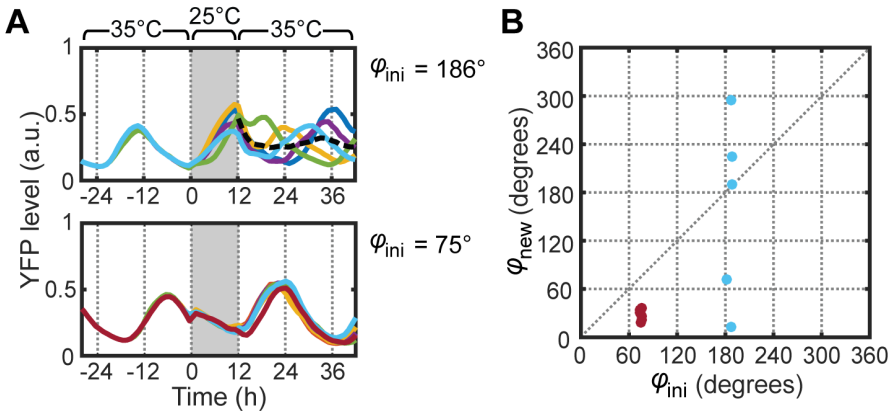

Figure 6. Stochastic vs. deterministic phase resetting responses to a 12 h 25°C pulse at 35°C. **(A)** Example YFP reporter traces of individual cellular clocks that illustrate stochastic (top, with an average $\varphi_{\mathrm{ini}} = 186°$) vs. deterministic (bottom, $\varphi_{\mathrm{ini}} = 75°$) responses to a 12 h shift to 25°C (represented by gray bar) applied at different initial phases. The reporter level is measured in arbitrary units (a.u.). Each diagram plots the automatically tracked daughter cells that are descended from the same mother cell at $t = -28$ h at 35°C, with the shift to 25°C set to $t = 0$. Because the clock runs independently of the cell cycle and its state is faithfully inherited at cell division (Yang et al., 2010), the clock dynamics can be continuously traced through cell lineages. (Top) The dashed black line shows the average of individual traces after the 25°C pulse. **(B)** Steady-state phase resetting responses plotted as φ_{ini} vs. φ_{new} data points, in light blue and red respectively for cells in the top and bottom panels in **(A)**.

(Fig. 7, 12 h). In addition to phase shifts, we also observed a transient φ_{ini}-dependent change in the oscillatory amplitude following the pulse (Fig. 8, see Methods for detailed analysis). In particular, some cells around $\varphi_{\mathrm{ini}}\sim186°$ (~10% cells within the 186°±20° φ_{ini} range, indicated with the yellow oval in Fig. 8B, with corresponding data points highlighted in yellow in Fig. 8A, C), where desynchronization is induced, exhibit an obvious amplitude reduction in the first day following transfer to 35°C, but then recover amplitude in the subsequent 26 h time window. Averaging the desynchronized YFP reporter traces would then generate attenuated oscillations following the 25°C pulse (exemplified by the colony in Fig. 6A, dashed black line). Therefore, for the cyanobacterial clock, the population-level damping of oscillations is not the result of suppression of circadian rhythms in individual clocks, but instead, of desynchronization among them. In addition to a 12 h shift to 25°C applied at $\varphi_{\mathrm{ini}}\sim186°$, the other critical perturbations

found to induce desynchronization are: a 15 h shift to 25°C applied at φ_{ini}~166°, an 18 h shift to 25°C applied at φ_{ini}~122°, a 21 h shift to 25°C applied at φ_{ini}~83°, and a 24 h shift to 25°C applied at φ_{ini}~55° (Fig. 7). A 9 h shift to 25°C applied at φ_{ini}~238° appears to be a threshold case, for it causes a steep shift in φ_{new} with minor divergence (Fig. 7). We observed deterministic behavior for all 3 h and 6 h shifts to 25°C at all φ_{ini} (Fig. 7).

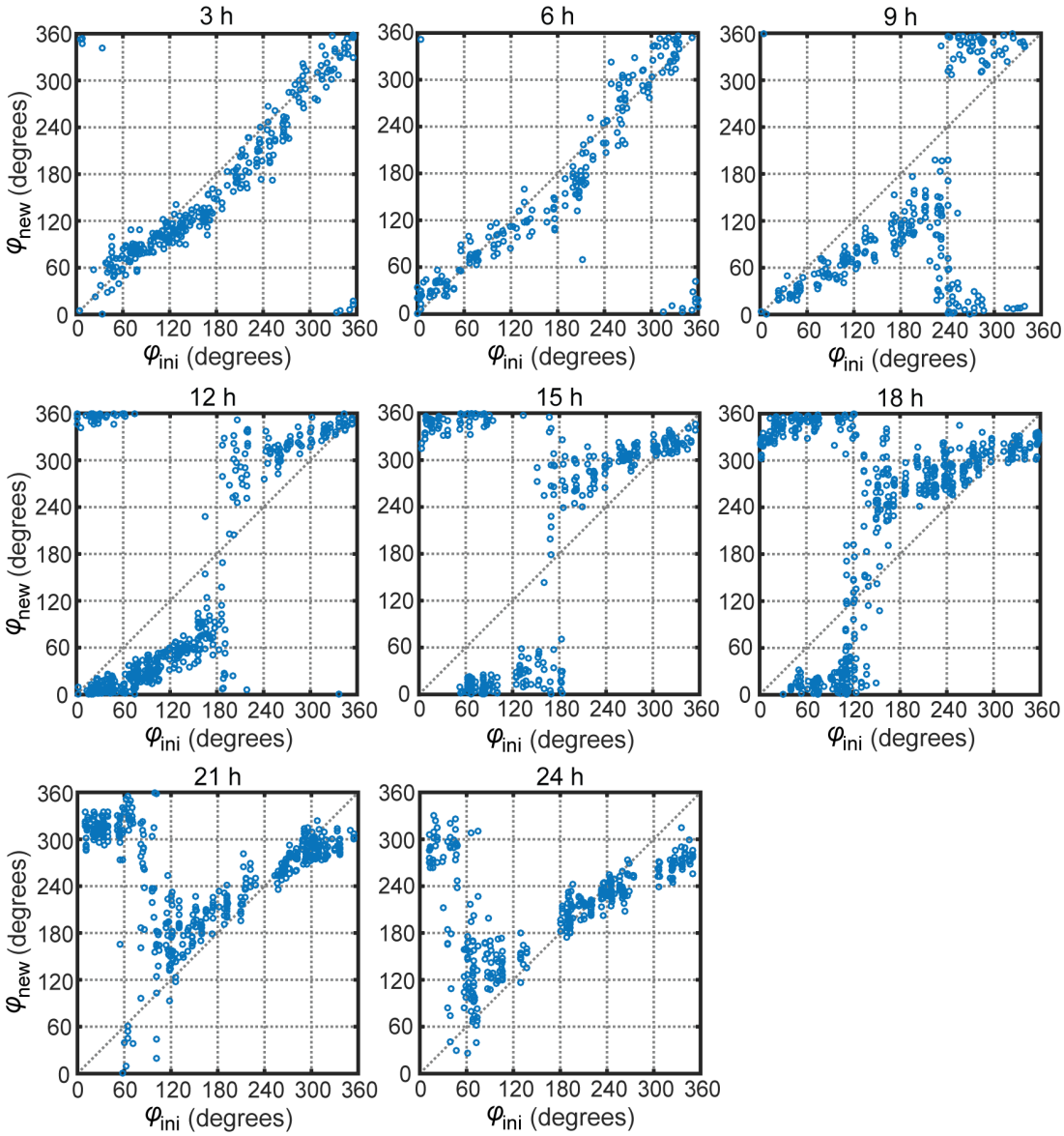

Figure 7. PTCs of 3 h to 24 h 25°C pulses.

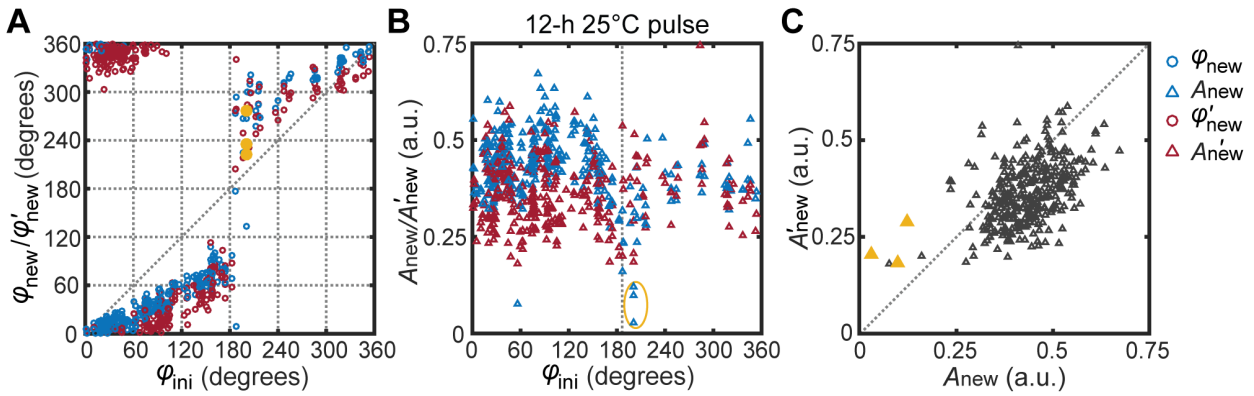

Figure 8. Analysis of the single-cell phases and amplitudes for one experiment of the 12 h 25°C pulse at 35°C. Two 26 h-long time windows – an earlier 6 h-32 h vs. later 22 h-48 h following the end of the pulse – were used to extract the post-pulse phases and amplitudes, respectively denoted by φ_{new} and A_{new} vs. φ'_{new} and A'_{new}. The amplitude is measured in arbitrary units (a.u.). **(A)** The single-cell PTC of φ_{ini} vs. φ_{new} (blue circles) or φ'_{new} (red circles). **(B)** The single-cell dependence of A_{new} (blue triangles) and A'_{new} (red triangles) on φ_{ini}. The critical φ_{ini} at stochastic phasing (i.e. spread of red and blue circles in **(A)**) is indicated by the dashed gray line. The individual cells with small A_{new} values are identified with yellow ovals, with their corresponding φ_{ini} vs. φ'_{new} and A_{new} vs. A'_{new} data points highlighted in yellow in **(A)** and **(C)**. **(C)** A_{new} vs. A'_{new} of all individual cells.

2.2 The clock state at the end of the perturbation determines whether the new phase is deterministic or stochastic

Given that stochastic phases can be induced by different combinations of pulse duration and the time the pulse was applied, we went on to ask whether these critical perturbations share any common features. We discovered that the clock state upon returning to 35°C is the dominant predictor of whether the new phase at 35°C is deterministic or stochastic. First, in response to the critical perturbations, the individual clocks oscillate with synchronized, deterministic dynamics during the 25°C pulse, and only upon restoring the temperature to 35°C do they become desynchronized with a new stochastic phase (Fig. 9). Also, despite the different lengths of the 25°C pulse in these perturbations, the YFP reporter level always comes close to reaching its peak at the end of the pulse. Thus, the five critical perturbations all drive the clock to a similar state at the end

of the 25°C pulse, but through different deterministic trajectories during the pulse (Fig. 9).

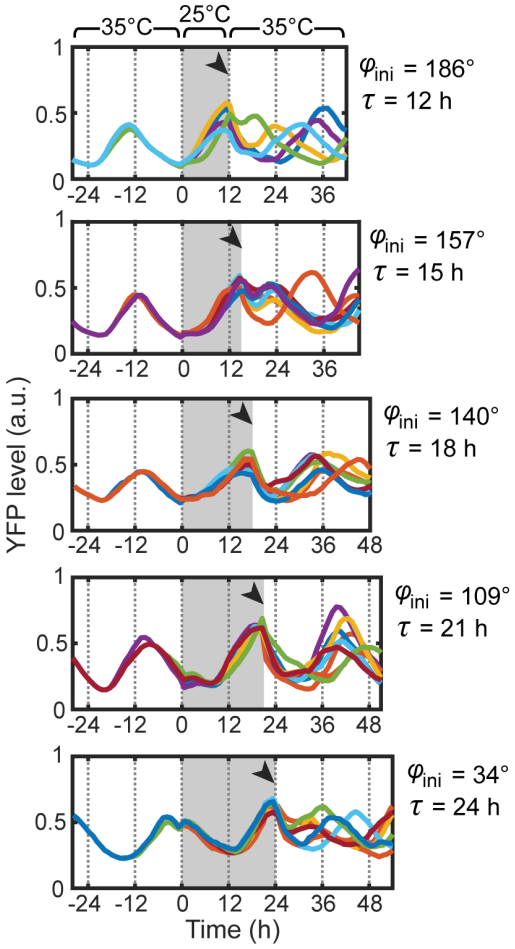

Figure 9. Example YFP reporter traces showing the stochastic phase resetting responses to various critical 25°C-pulse perturbations (τ and average φ_{ini} labeled in the diagram). The YFP reporter level at the end of a 25°C pulse is highlighted by black arrow.

A 25°C pulse in a 35°C background is essentially two successive temperature shifts – first from 35°C to 25°C and then from 25°C to 35°C. Therefore, the responses to 25°C pulses can be used to predict phase resetting by these two temperature shifts and suggest that: (1) shifting the temperature from 35°C to 25°C will result in slight deterministic modulation of the circadian phase independent of when the temperature shift occurs (see Methods); and (2) shifting the temperature from 25°C to 35°C can induce stochasticity in the phase of oscillations at 35°C, if the shift is

applied when the YFP reporter of the clock at 25°C reaches near its peak. To test these predictions, we measured the single-cell PTC for a 35°C-to-25°C temperature step-down, and for a 25°C-to-35°C temperature step-up. To quantify the steady-state responses to a temperature shift, the before-shift and after-shift phases (φ_{bf} and φ_{af}) of the clock are measured by identifying the phases of stable circadian oscillations before and after the temperature shift, referenced to the state of the clock at the time of shift – the actual clock state for φ_{bf}, and the extrapolated state for φ_{af} (Fig. 10, blue and red arrows, respectively). The single-cell PTC of the 35°C-to-25°C shift displays a

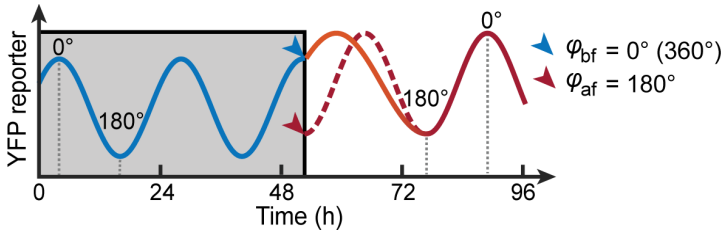

Figure 10 Schematic of the quantification of a clock's phase before and after a temperature shift (φ_{bf} and φ_{af}). The dashed red line denotes tracing the post-shift rhythms that are stabilized after a period of transient dynamics (red line following orange line) back to the time of temperature shift. In this example plot, the clock is reset from $\varphi_{\mathrm{bf}} = 0°$ (blue line at its peak) to $\varphi_{\mathrm{af}} = 180°$ (dashed red line at its trough).

tight distribution close to the line of $\varphi_{\mathrm{bf}} = \varphi_{\mathrm{af}}$ (Fig. 11A; diagonal dashed line), confirming the

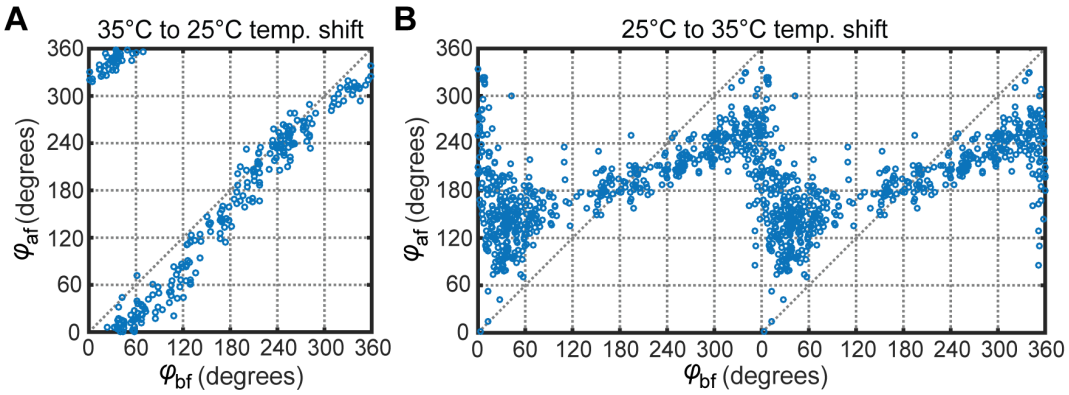

Figure 11 (Continued). PTCs plotting φ_{bf} vs. φ_{af} relationship of individual cellular clocks being transferred **(A)** from 35°C to 25°C and **(B)** from 25°C to 35°C (double plotted to demonstrate the divergence in φ_{af} at φ_{bf}~0°).

predicted deterministic modulation of circadian phase. In response to the 25°C-to-35°C shift, the after-shift amplitude stabilizes following a transient change (Fig. 12), confirming the persistence of robust oscillations at 35°C; while the PTC's scattering in φ_{af} at φ_{bf}~0° (corresponding to the maximum YFP reporter level; Fig. 11B) demonstrates the induction of stochastic phases, if the clock running at 25°C is shifted to 35°C when the YFP reporter is close to its peak (example YFP reporter traces shown in Fig. 13). These observations provide additional support for the notion that the dominant predictor of stochastic phases at 35°C is bringing the clock to the single critical state upon returning to 35°C; the oscillatory trajectories taken to this state do not matter and can differ.

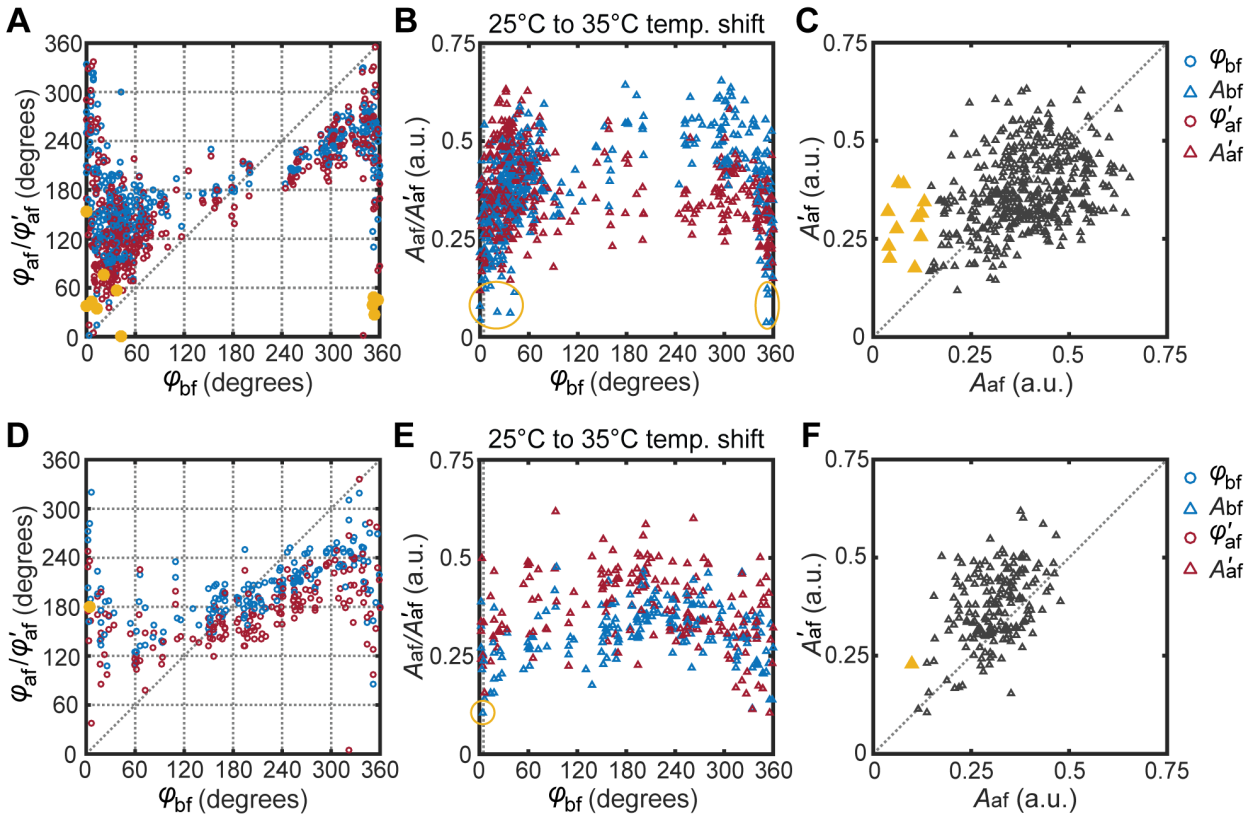

Figure 12 (Continued). The two sets of diagrams – **(A) (B) (C)** and **(D) (E) (F) –** present analysis of the single-cell phases and amplitudes for two individual experiments of the 25°C-to-35°C shift, which were combined to generate the PTC shown in Fig. 11B. The phases and amplitudes extracted from an earlier vs. later 26 h-long time window (6 h-32h vs. 22 h-48 h) after the temperature shift are respectively denoted by φ_{af} and A_{af} vs. φ'_{af} and A'_{af}. Each set of diagrams are equivalent to those elaborated in Fig. 8, and thus not explained in further detail here. Consistently, cells that experience a transient reduction in their oscillatory amplitudes are highlighted in yellow.

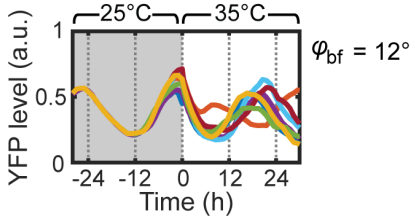

Figure 13. Example YFP reporter traces showing the induction of stochastic phases by shifting temperature from 25°C to 35°C when the YFP reporter comes close to its peak at 25°C, corresponding to $\varphi_{\mathrm{bf}}\sim 0°$.

2.3 A limit cycle framework for interpreting phase resetting responses

We reasoned that our understanding of the cyanobacterial clock as an oscillator (Strogatz, 2001; Winfree, 2010) and the proposed predictor of deterministic vs. stochastic phases should be sufficient to explain our experimental data, and turned to mathematical modeling to test this. Conceptually, given a clock running in constant environmental conditions (called 'free-running'), circadian rhythms arise from the state of the clock cycling along a closed trajectory, called a 'limit cycle' (Fig. 14, black circle) (Strogatz, 2001), in the space characterized by clock proteins' abundance and modifications. There exists at least one steady state inside this limit cycle; in addition, the clock system might have other periodic or steady-state solutions (Strogatz, 2001). For the cyanobacterial clock, the simplest and also most likely scenario consists of one unstable steady-state point (termed a 'singularity'; Fig. 14, black dot at the center) residing inside a globally stable limit cycle (Fig. 14, black circle), meaning that if transiently perturbed off the limit cycle to any state point except for the unstable singularity, the clock would restore its stable oscillations and

relax back into the limit cycle (Fig. 14, gray trajectories projecting from the yellow dot and the light blue dot; Methods) (Qin et al., 2010). In reality, the limit cycle of a clock system has many

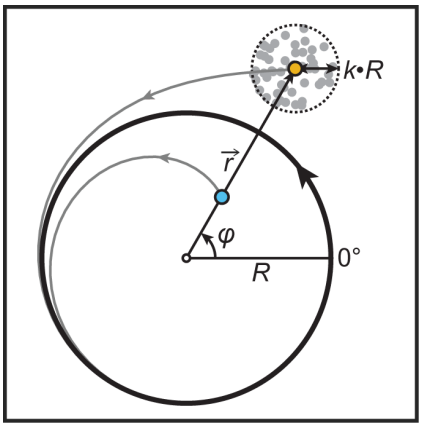

Figure 14. Diagram that illustrates modeling stable circadian oscillations as a two-dimensional circular limit cycle (black circle) centered at the unstable singularity (black dot at the center). For a clock starting to free-run from an off-limit-cycle state (e.g. yellow or light blue dot), the gray line represents the transient trajectory along which the clock is attracted into the limit cycle. The cluster of gray dots demonstrate the distribution of states that the clock at the yellow dot can be displaced to by random noise, and in this illustration, they were generated with the value $k = 0.3$. They also mimic a group of approximately synchronized cells with minor cell-to-cell variation in their clock states.

dimensions, because each protein state is one dimension. To build a concise conceptual model, however, we can continuously map the states in the multidimensional space onto a two-dimensional plane (Hubbard and West, 1995), so that a free-running clock spirals into and along a circular limit cycle (Fig. 14, black circle) centered at the unstable singularity (black dot) with constant counterclockwise angular velocity. In other words, the dynamics of the clock system along the angular direction (φ) are uncoupled from the radial direction (r); and then clocks running from state points along a radial axis (variable r but same φ; Fig. 14, e.g. yellow and light blue dots along black line) will eventually become synchronized after they have spiraled into the limit cycle, and thus share the same steady-state phase φ independent of r. Mathematically, this mapping is

called ‘homeomorphic transformation’ (Hubbard and West, 1995). Not yet considering stochastic phase resetting responses, the distribution of single-cell data points along a PTC trend line is indicative of variation in the clock states among synchronized cells (Chabot et al., 2007; Mihalcescu et al., 2004; Teng et al., 2013). To account for variation in simulating single-cell responses, to a given noise-free clock state (Fig. 14, yellow dot) we add a random displacement that is uniformly distributed within a small disk centered at the noise-free state (Fig. 14, gray dots around the yellow dot at the center); the radius of the small disk ($k \cdot R$) is assumed to be proportional to the limit cycle radius (R) with ratio k (Fig. 14).

2.4 Temperature resets the clock by modulating the geometric structure of limit cycle

Having set up the limit cycle framework, we then sought to model resetting behavior based on it, and as a first step, to recapitulate the responses to temperature shifts for they are the simplest, most reduced signal. As a system parameter of the clock, temperature affects circadian oscillations predominantly by modulating the asymptotic orbit, i.e. the limit cycle, towards which a free-running clock relaxes (Gooch, 2007; Peterson, 1980b), as supported by the variable oscillatory trajectories of a free-running clock at 25°C vs. at 35°C (Fig. 15, Methods). In contrast, temperature

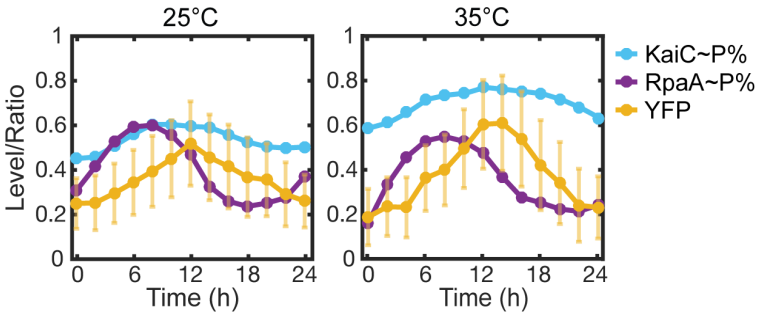

Figure 15. Variable circadian rhythms at 25°C vs. 35°C measured in a synchronized population by (1) the ratio of KaiC phosphorylation (KaiC~P%, including all three phosphoforms – T-KaiC, ST-KaiC, and S-KaiC), (2) the ratio of RpaA phosphorylation (RpaA~P%), and (3) the distribution

(Continued) of single-cell YFP reporter level which is presented as mean with standard deviation. The rhythms at 25°C vs. 35°C indicate that temperature modulates free-running oscillatory trajectories.

only slightly alters the oscillatory period (e.g. $T_{25°C} = 24.7$ h, $T_{35°C} = 25.2$ h, Methods) (Kondo et al., 1993). Since a temperature signal is composed of change(s) in temperature, it resets the clock by switching the limit cycle it spirals into or around throughout the signal. For example, in response to a shift from temperature 1 to 2, if denoting the limit cycle characteristic of stable free-running oscillations at temperature 1 as 'LC_1' and that at temperature 2 'LC_2' (Fig. 16; blue circle LC_1 and red circle LC_2, whose relative geometry is defined by the parameters $d_{1,2}$, R_1, R_2, α_{1-2}, α_{2-1} as illustrated), the clock originally running along LC_1 will, starting from certain state on it (yellow dot on blue circle LC_1), spiral towards LC_2 upon the shift. Equivalent to how we experimentally

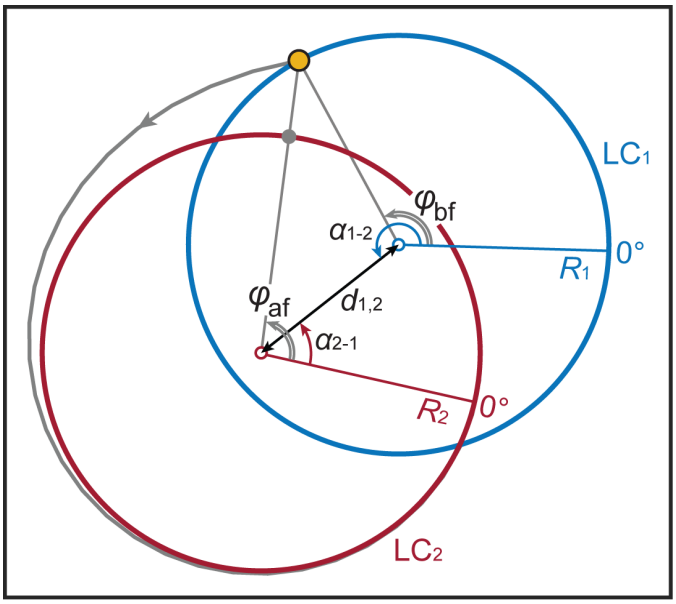

Figure 16. Generic representation of the geometric relationship between limit cycles of two temperatures (LC_1 and LC_2), and the quantification of φ_{bf} and φ_{af} in shifting temperature from 1 to 2. The parameters used to describe the relative geometry between LC_1 and LC_2 are: (1) the radius of LC_1 (R_1) and that of LC_2 (R_2), (2) the distance between the unstable singularities, i.e. centers of LC_1 and LC_2 ($d_{1,2}$), (3) the angle from the 0° direction of LC_1 to the singularity at temperature 2 (α_{1-2}), and that from the 0° direction of LC_2 to the singularity at temperature 1

(Continued) (α_{2-1}). The 0° direction of either limit cycle corresponds to the clock state experimentally defined as 0° by the peak of the YFP reporter.

determined the steady-state phases from a YFP reporter trace, in our model, φ_{bf} and φ_{af} should be the angular coordinates of the clock state at the time of temperature shift, respectively, in reference to LC_1 and to LC_2 (gray lines connecting the singularities and yellow dot); and the transition from φ_{bf} and φ_{af} arises from the displacement of singularity ($d_{1,2}$) relative to the limit cycle of before-shift temperature LC_1. Given this simple relationship, without considering noise, the dynamical question of computing steady-state phase resetting responses is amenable to trigonometric reasoning. We can thus analytically derive φ_{af} as a function of φ_{bf} for the shift from temperature 1 to 2, and similarly for the reverse shift from temperature 2 to 1 (equations in Methods). Fitting the derived φ_{bf} vs. φ_{af} functions to the measured PTCs of 1-to-2 and 2-to-1 shifts can thus constrain the relative geometry between LC_1 and LC_2.

Applying this analysis to the 25°C-to-35°C and 35°C-to-25°C data (Fig. 17, Methods) yielded $LC_{25°C}$ and $LC_{35°C}$ as graphically presented in Fig. 18 (blue circle $LC_{25°C}$ with its radius $R_{25°C}$ arbitrarily set to 1, and red circle $LC_{35°C}$ scaled proportionally as described in Methods). Such

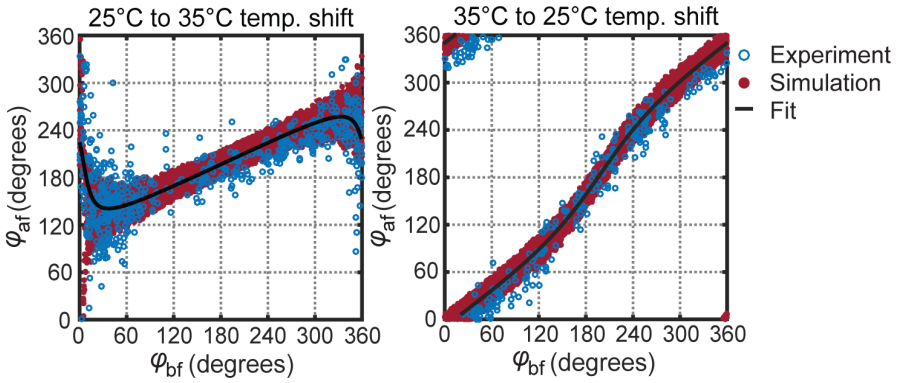

Figure 17. Fitting the single-cell PTCs (experimental data shown as blue circles) of temperature

(Continued) shifts between 25°C and 35°C. The black curve shows the analytically derived noise-free PTC used to least-square-fit the deterministic part of single-cell PTCs. Red points indicate the single-cell responses simulated with noise. These plotting symbols (blue circle, black curve, and red point) are kept consistent in all following figures.

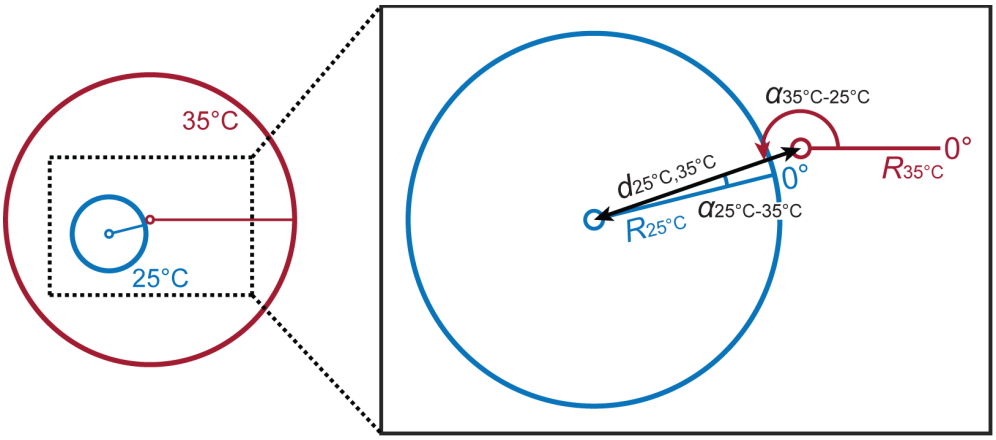

Figure 18. Fitted relative geometry between $LC_{25°C}$ (blue circle) and $LC_{35°C}$ (red circle). For each temperature, also plotted in matching color is a dot at the center representing the unstable singularity, and connected to it, a straight line marking the reference direction of 0° phase. Magnified details are shown in the box.

geometric relationship dictates that the 5° phase point on $LC_{25°C}$ lies very close to the 35°C unstable singularity (Fig. 19A). Considering the noise term that describes cell-to-cell variation in clock states, for a group of synchronized cells with $\varphi_{bf} = 5°$, rather than locating exactly on the same point on $LC_{25°C}$, their clock states form a small cluster around it, covering the 35°C unstable singularity and expanding the full range of angular coordinates in reference to $LC_{35°C}$ (Fig. 19A, light blue dots). Upon shifting temperature to 35°C, these states will then relax into $LC_{35°C}$ with divergent phases (Fig. 19A, orange dots). This explains our observation that releasing the clock into 35°C from a single critical state elicits stochastic phases, and suggests that this critical state is the unstable singularity of the clock at 35°C (Fig. 19A, red dot). In contrast, if the temperature is shifted from 25°C to 35°C at $\varphi_{bf} = 90°$ for example (Fig. 19B, light blue dots), because the clock states are farther away from the 35°C singularity, the range of angular coordinates expanded by

the same size of cluster of clock states is much smaller, resulting in a tight distribution in φ_{af} around a deterministic value (Fig. 19B, orange dots).

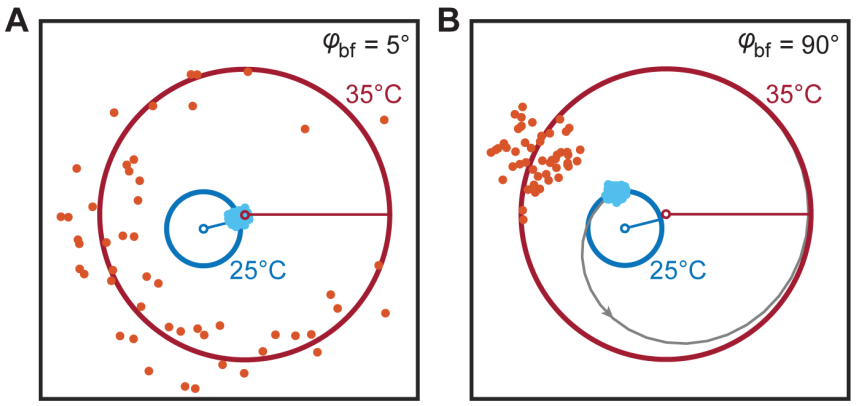

Figure 19. Simulated single-cell responses to a 25°C-to-35°C shift applied at **(A)** $\varphi_{bf} = 5°$ vs. **(B)** $\varphi_{bf} = 90°$. For a group of individual cellular clocks ($n = 50$), light blue dots mark their states at the time of temperature shift, while orange dots denote, in one randomized simulation, where they arrive after running for one free-running period of time (25.2 h) at 35°C. **(B)** A gray line is also plotted to represent how the approximately synchronized clocks relax towards $LC_{35°C}$ throughout this period of time.

2.5 Recapitulating phase resetting by 25°C pulses further confirms that the unstable singularity underlies stochastic responses

With the limit cycle geometry constrained by the responses to temperature shifts, we then went on to model phase resetting by the more complicated signal of low-temperature pulses (composed of two successive temperature shifts). In response to a 25°C pulse at 35°C, clock oscillations will change from $LC_{35°C}$ before the pulse to $LC_{25°C}$ during the pulse, and then back to the original $LC_{35°C}$ after the pulse. Because this process involves spiraling towards $LC_{25°C}$ for different lengths of time in our experiments, to fit the data we need to describe the relaxation dynamics of the clock. For this, we chose the *Poincaré* oscillator (Beuter et al., 2003) which adopts the simplest form of differential equations that can also implement previous simplifications made to set up the model

(i.e. circular limit cycle and constant angular velocity) (see Methods for a detailed discussion of the assumptions and simplifications made in our model). In the frame of reference of either temperature, with the relaxation coefficient ε, the clock dynamics are described by $\frac{dr}{dt} = -\varepsilon r(R - r)$, $\frac{d\varphi}{dt} = \frac{2\pi}{T}$. r monotonically approaches R with $r = \frac{1}{\left(\frac{1}{r_0} - \frac{1}{R}\right)\mathrm{e}^{-\varepsilon R t} + \frac{1}{R}}$ ($r = r_0$ at $t = 0$). To determine ε, for each pulse duration (3 h, 6 h, … 24 h), we simulated the phase resetting processes without adding any noise, quantified φ_{ini} and φ_{new} in a manner similar to that employed to analyze the experimental results, and thus obtained a series of theoretical PTCs of 25°C pulses. Least-square-fitting these PTCs to all deterministic phases resetting responses together gives a relaxation timescale, $\varepsilon = 0.32\ \mathrm{h}^{-1}$ (Fig. 20, Methods).

To intuitively understand how pulse duration and initial phase at the pulse determine whether the new phase is stochastic or deterministic, we plotted trajectories of the clock state to visualize what happens throughout the phase resetting process. In relaxing towards $LC_{25°C}$, multiple critical perturbations all have the appropriate combinations of pulse duration and initial phase at the pulse to bring the clock state close to the 35°C singularity at the end of the 25°C pulse (Fig. 21, gray lines converging on the red dot), while the other perturbations do not (one example shown in Fig. 22A). The dynamical properties of the clock govern all phase resetting responses, but in our model, are constrained by fitting the deterministic responses. Therefore, simulation of these critical perturbations that were not used to constrain the relaxation timescale ε can corroborate the notion that a critical state – the 35°C unstable singularity – underlies the stochastic phasing at 35°C, while the trajectories taken to the 35°C unstable singularity do not matter. In addition, the PTCs of the pulses that clearly elicit stochastic phase resetting responses (12 h to 24 h) display a steep ~180°

shift in φ_{new} upon small variation in φ_{ini} around the critical phase at stochastic response (Fig. 20). Taking the simulated critical perturbation of a 12 h pulse at $\varphi_{\mathrm{ini}} = 203°$ (whose value is determined by where the slope of fitted PTC is steepest, black curve in Fig. 20) for example (Fig. 22B, middle), if the pulse is applied at a slightly earlier phase $\varphi_{\mathrm{ini}} = 183°$ (Fig. 22B, top) or at a

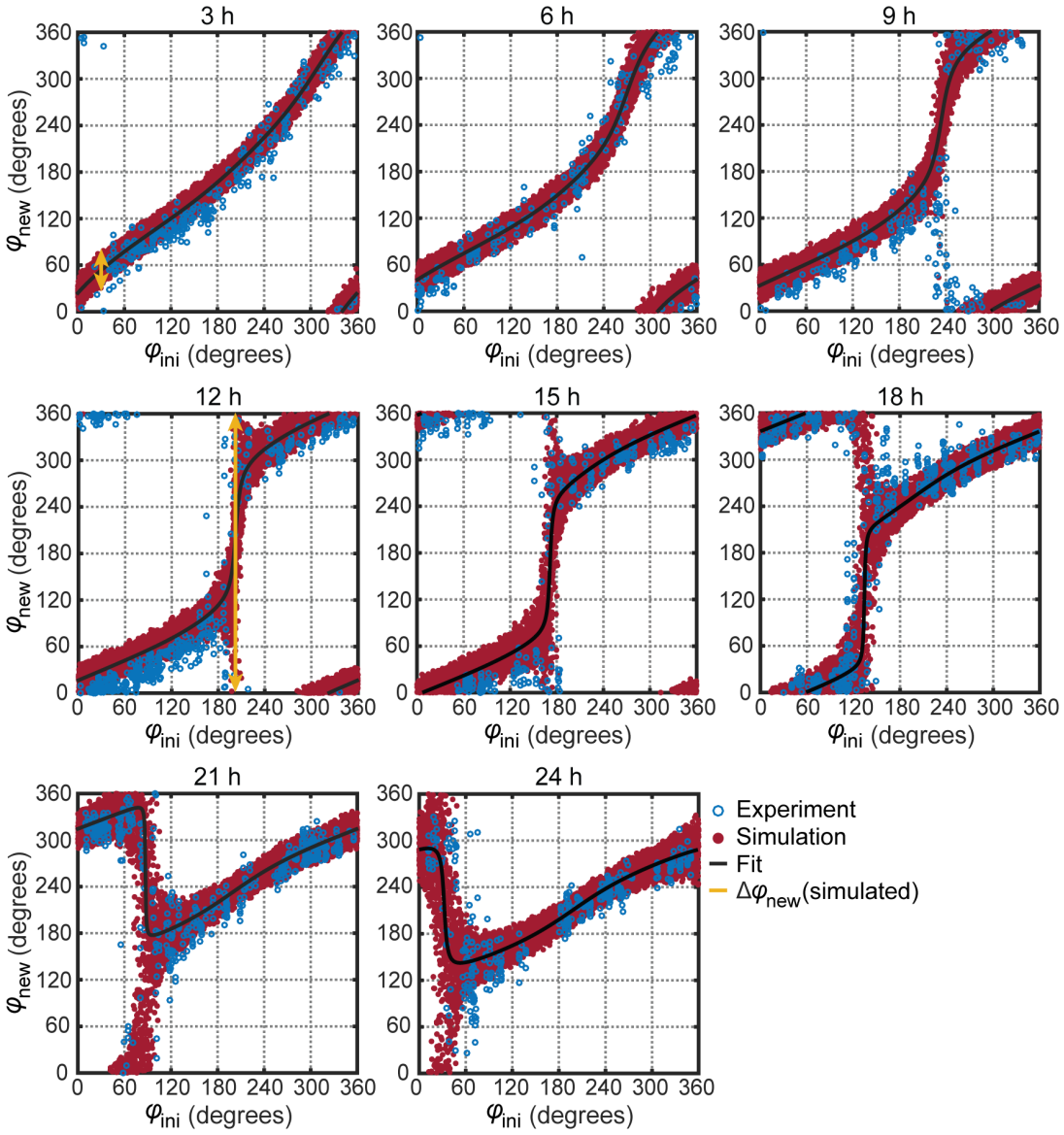

Figure 20. Fitting the single-cell PTCs of 25°C pulses at 35°C. The yellow lines illustrate, in response to a particular 25°C pulse, the quantification of maximum spread of φ_{new} between cells with similar φ_{ini} ($\Delta\varphi_{\mathrm{new}}$), which is used to plot Fig. 27B.

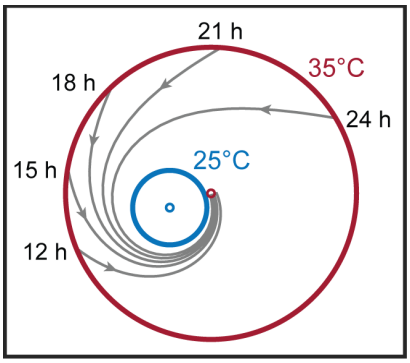

Figure 21. Simulated clock-state trajectories throughout the 25°C pulse (gray lines) in response to the critical perturbations that induce stochastic phases. The critical perturbations are: 12 h 25°C pulse at $\varphi_{\mathrm{ini}} = 203°$, 15 h at $\varphi_{\mathrm{ini}} = 171°$, 18 h at $\varphi_{\mathrm{ini}} = 134°$, 21 h at $\varphi_{\mathrm{ini}} = 87°$, and 24 h at $\varphi_{\mathrm{ini}} = 32°$. Here, the value of φ_{ini} is computed by where the slope of a fitted PTC is steepest (black curves in Fig. 20).

later phase $\varphi_{\mathrm{ini}} = 223°$ (Fig. 22B, bottom), though physically close to each other, the clock states at the end of the 25°C pulse (Fig. 22B, top center $\varphi_{\mathrm{ini}} = 183°$, bottom center $\varphi_{\mathrm{ini}} = 223°$; black dots close to red dot at the center) are located at two opposing radial axes across the singularity of the 35°C limit cycle (indicated by the dashed gray lines in the top center and bottom center diagrams), thus resulting in a ~180° difference in φ_{new} (Fig. 22B, top right $\varphi_{\mathrm{ini}} = 183°$, bottom right $\varphi_{\mathrm{ini}} = 223°$; black dots on red circle).

To examine the threshold in pulse duration (~12 h) for inducing stochastic phases for a 25°C pulse, we plotted the end-of-25°C-pulse states for pulses applied at all initial phases (Fig. 23). As the ring of end-of-pulse state distribution converges towards the 25°C limit cycle with increasing pulse duration (Fig. 23), it passes through the singularity at 12 h and then remains close to it, meaning that there exists a particular initial phase at which any no-shorter-than-12 h pulse applied can bring

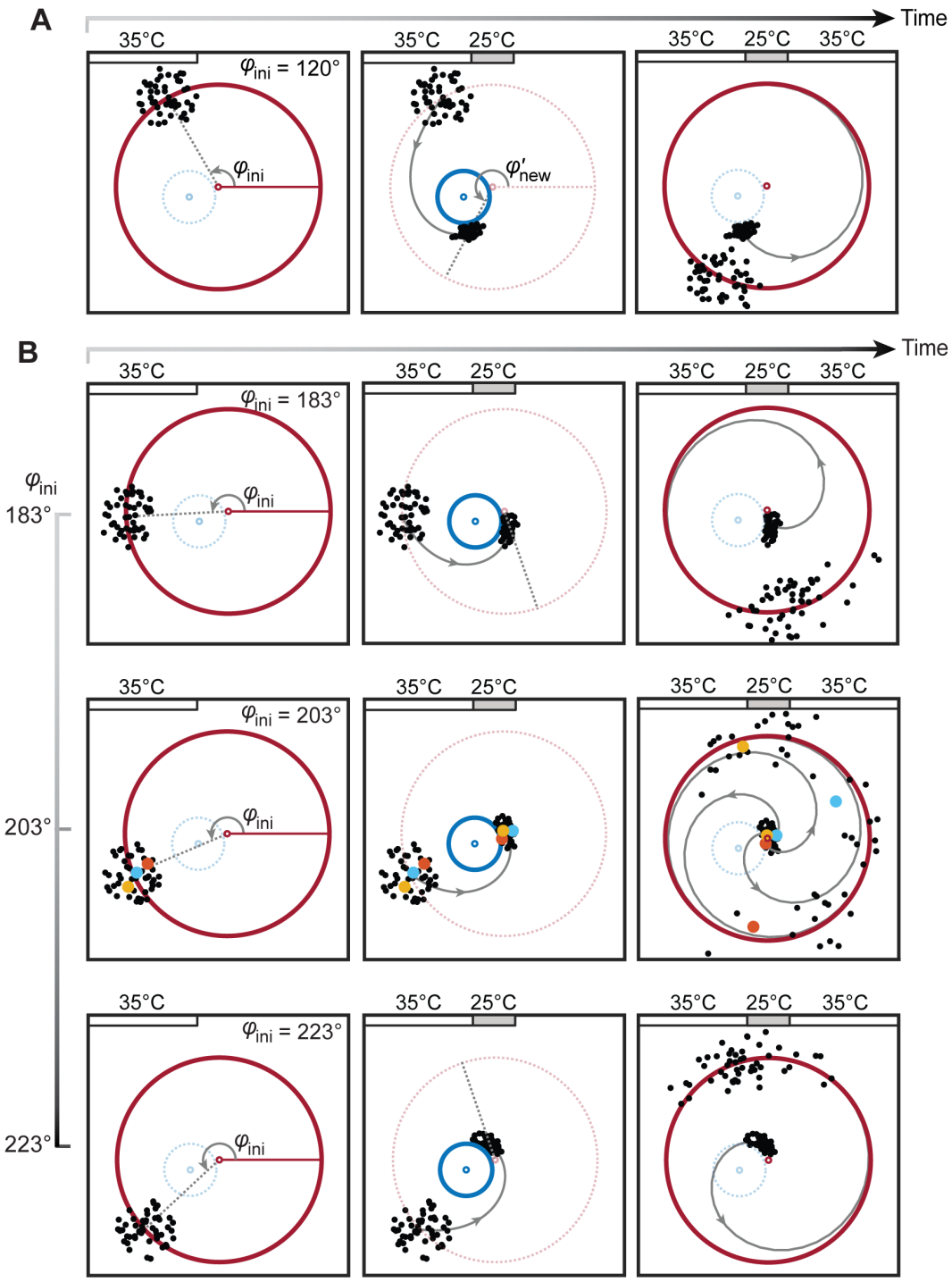

Figure 22. Simulated single-cell phase resetting processes in response to a 12 h pulse applied at **(A)** $\varphi_{ini} = 120°$ and **(B)** $\varphi_{ini} = 183°$ (top panel), 203° (middle), and 223° (bottom). Each panel is dissected into three sequential diagrams illustrating the clock originally free-running at 35°C, shifting to 25°C, and lastly, returning to 35°C: (left) a cluster of clock states (black dots) with certain average φ_{ini} at the onset of 25°C pulse; (center) in relaxing towards $LC_{25°C}$, the trajectory (gray line) that takes the clocks from these states to where they are at the end of the pulse (black dots at the end of gray line); (right) the trajectory (gray line) along which the clocks spiral back

(Continued) into $LC_{35°C}$, and the states they traverse after one free-running period of time (25.2 h) at 35°C (black dots along $LC_{35°C}$). In each diagram, only the limit cycle the clock should spiral into or around (left $LC_{35°C}$, middle $LC_{25°C}$, right $LC_{35°C}$) is shown in solid line, and the other one is semi-transparent. **(A)** φ'_{new} is labeled as defined in Methods. **(B)** In the middle panel featuring the fitted critical perturbation of a 12 h pulse at $\varphi_{\mathrm{ini}} = 203°$, three clocks are color-coded to assist tracking them throughout the phase resetting process. In the left and center diagrams, the dashed gray line highlights the average radial axis on which certain cluster of clock states are located.

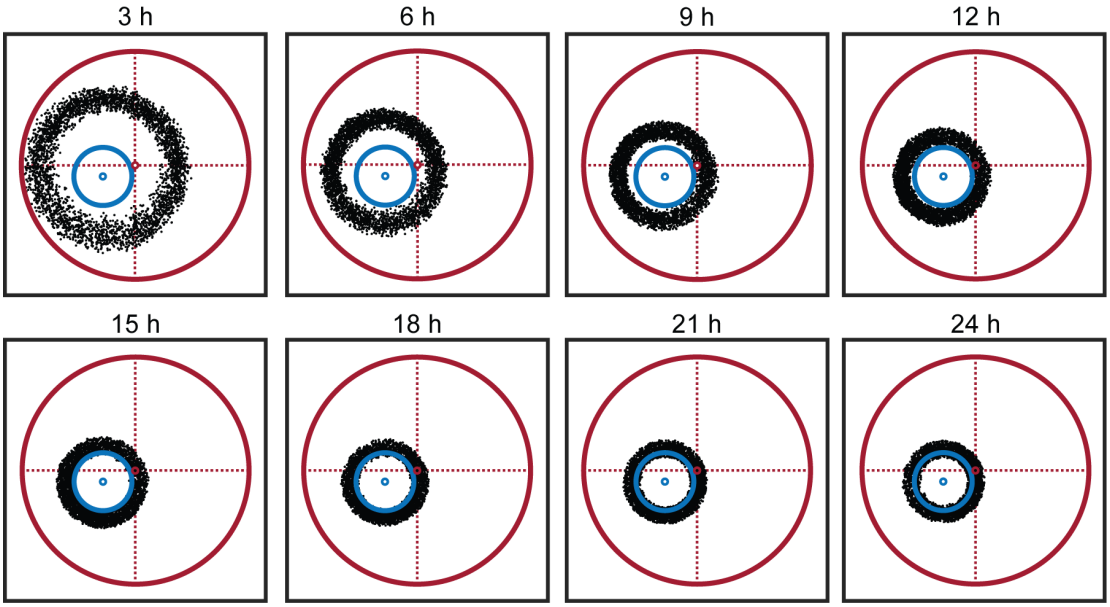

Figure 23. Simulated single-cell distribution of end-of-pulse clock states for all lengths of pulses. Two perpendicular dashed red lines are plotted to indicate the position of the 35°C singularity at their intersection.

clock state to the vicinity of the 35°C singularity at the end of it. Because this trend requires that $LC_{25°C}$ does not enclose but lies close to the 35°C singularity, the existence of pulses that can induce stochastic phases and this threshold effect of pulse duration is specific to the relative geometry between $LC_{25°C}$ and $LC_{35°C}$. The threshold value also depends on the relaxation timescale – the faster the clock relaxes to $LC_{25°C}$, the shorter time it takes to approach the 35°C singularity.

Moreover, this model can explain the transient amplitude reduction that may occur with stochastic phasing (Fig. 8, 12). Specifically, although it is unclear how the oscillatory amplitude of the YFP

reporter corresponds to the radius (r) of a clock state in our conceptual model, it is safe to assume that their values are positively correlated. Thus, the radial relaxation of a simulated clock state can be used to qualitatively infer the stabilization of the YFP reporter level. As the radial relaxation is described by $r = \frac{1}{\left(\frac{1}{r_0}-\frac{1}{R}\right)e^{-\varepsilon R t}+\frac{1}{R}}$ ($r = r_0$ at $t = 0$), if a clock starts oscillating from the vicinity of the unstable singularity ($r_0 \sim 0$), which underlies the stochastic phasing, the time (t_1) it takes to reach a certain radius (r_1, say $0.9R$) is: $t_1 = \frac{1}{\varepsilon R}\ln\left(\frac{r_1}{r_0}\cdot\frac{1-\frac{r_0}{R}}{1-\frac{r_1}{R}}\right) \approx \frac{1}{\varepsilon R}\ln\left(\frac{r_1}{r_0}\cdot\frac{1}{1-\frac{r_1}{R}}\right) \propto -\ln r_0$. t_1 sharply increases as r_0 approaches 0, meaning that if a clock happens to lie very close to the 35°C singularity at the end of a 25°C pulse, the stabilization of the oscillatory amplitude could be significantly delayed.

2.6 The geometric relationship between limit cycles of pulse- and background-temperatures govern the existence of stochastic responses to pulse signals

To generalize what we learned with the specific signal of 25°C pulses at 35°C and grasp the trend of temperature effects on circadian oscillations, we sampled additional temperatures (30°C – the midpoint between 25°C and 35°C, $T_{30°C} = 25.0$ h; and 37.5°C – the upper boundary of non-stressful temperatures, $T_{37.5°C} = 24.9$ h). We measured phase resetting by temperature shifts between 25°C, and 30°C and 37.5°C, respectively (Fig. 24), and as we did for 35°C, used these results to fit the geometry of the 30°C and the 37.5°C limit cycles ('$LC_{30°C}$' and '$LC_{37.5°C}$'), each in reference to $LC_{25°C}$ (Fig. 25, 26, green circle $LC_{30°C}$ and yellow circle $LC_{37.5°C}$; Methods). The higher-temperature singularity monotonically moves away with rising temperature, from inside (30°C, Fig. 25, small green circle) to outside (35°C, red dot; and 37.5°C, yellow dot) $LC_{25°C}$ (blue circle). Therefore, for 25°C pulses at higher temperatures, the pulse-temperature limit cycle, i.e.

$LC_{25°C}$, can either enclose, pass through, or exclude a background-temperature singularity depending on what temperature it is. Because the induction of stochastic phases by pulse signals

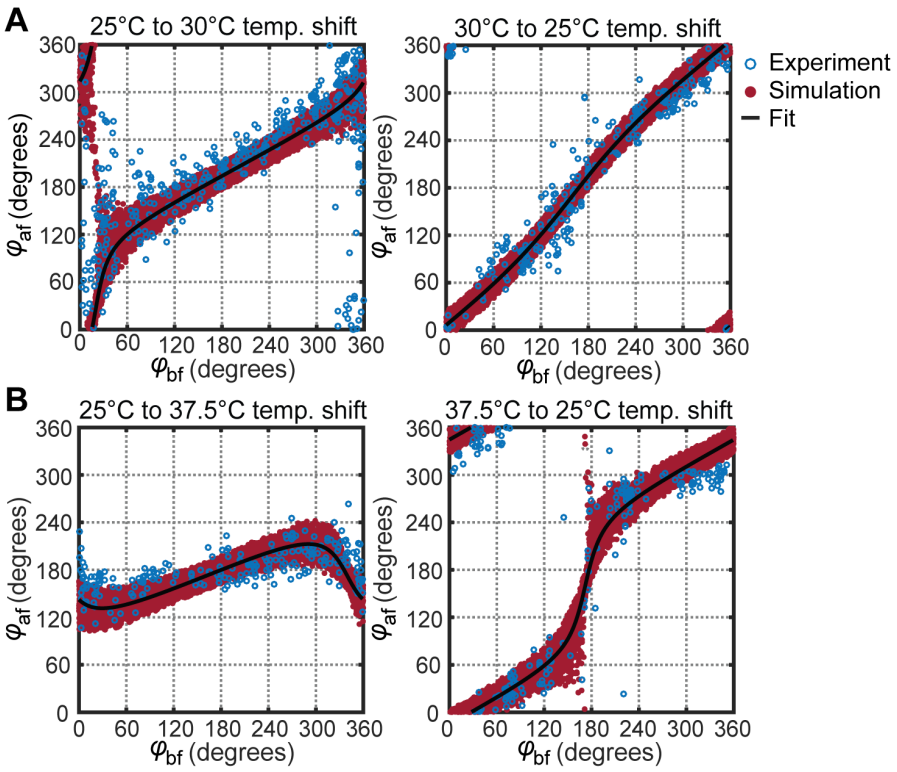

Figure 24. Fitting the PTCs of temperature shifts between **(A)** 25°C and 30°, and between **(B)** 25°C and 37.5°C, with ~28 h imaged before a shift.

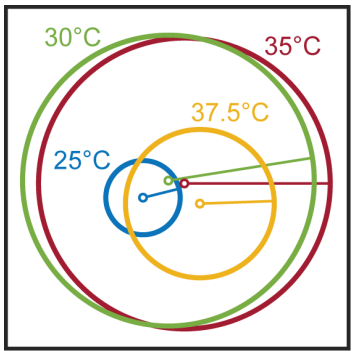

Figure 25. Diagram of $LC_{30°C}$ (green), $LC_{35°C}$ (red), and $LC_{37.5°C}$ (yellow), each defined relative to $LC_{25°C}$ (blue). The unstable singularity and 0° phase direction at each temperature are plotted in matching color.

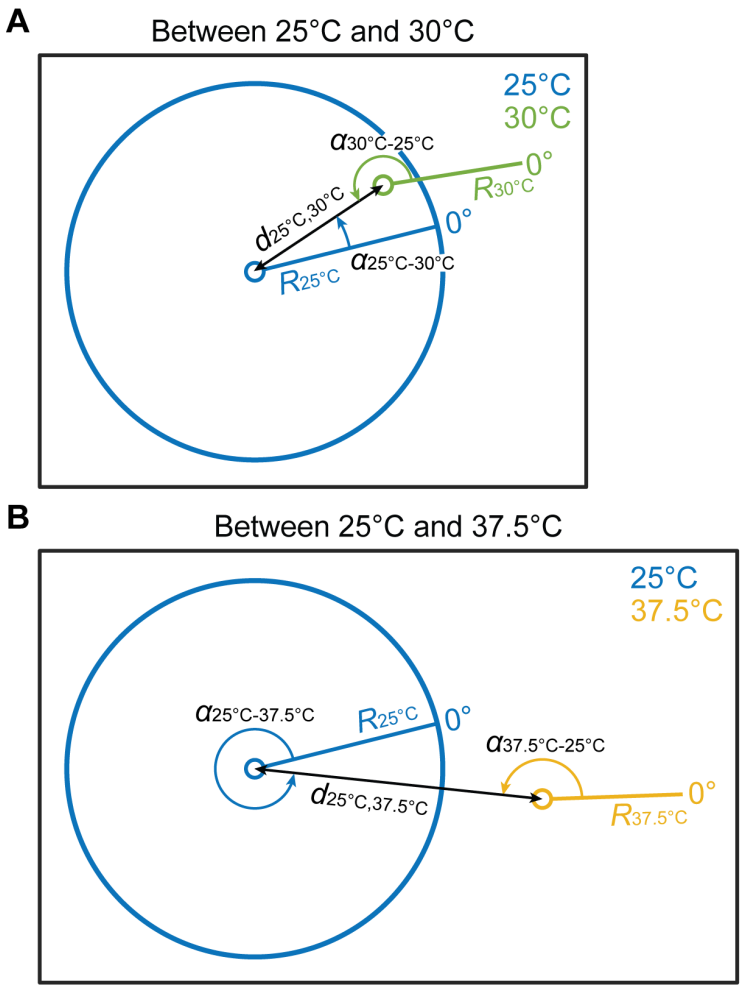

Figure 26. Magnified details of the fitted relative geometry **(A)** between $LC_{25°C}$ and $LC_{30°C}$, and that **(B)** between $LC_{25°C}$ and $LC_{37.5°C}$. Plotting symbols are the same as those used in Fig. 18 (for demonstrating the relative geometry between $LC_{25°C}$ and $LC_{35°C}$).

require that the clock can reach the background-temperature singularity in spiraling towards the pulse-temperature limit cycle, we explored how the relative position of the pulse-temperature limit cycle and the background-temperature singularity influences the nature of phase resetting responses (e.g. Fig. 27A, from left to right; blue circle enclosing, passing through, or excluding red dot). As a simple theoretical demonstration, we allowed $d_{25°C,35°C}$ to vary from $0.1R_{25°C}$ to $1.9R_{25°C}$ ($R_{25°C} = 1$), and scanned the responses to 25°C pulses of various duration (τ) to probe whether stochastic phasing can occur. We simulated the single-cell PTC to the 25°C pulse for each

pair of τ and $d_{25°C,35°C}$ values, and quantified the maximum spread of φ_{new} between cells with similar φ_{ini} (denoted by $\Delta\varphi_{new}$) – a small $\Delta\varphi_{new}$ indicates purely deterministic behavior (e.g. 3

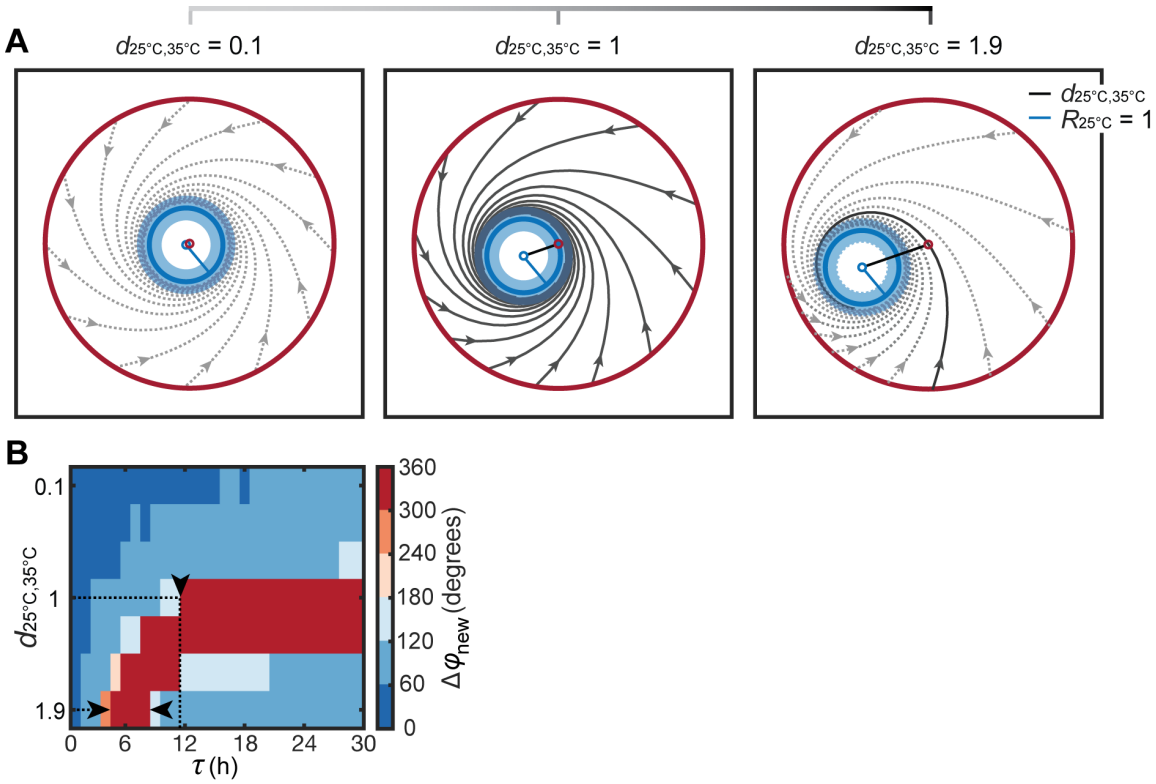

Figure 27. Exploring the possibility of inducing stochastic phases by pulse signals in general. **(A)** Plots of clock-state trajectories. The shaded blue ring neighboring $LC_{25°C}$ (blue circle) indicates the region where a clock stably running at 25°C can be distributed if considering the noise in clock state. The dashed gray lines denote potential trajectories along which the clock originally running along $LC_{35°C}$ (red circle) can spiral towards $LC_{25°C}$. Among them, highlighted in solid gray are the ones that can take a clock to the 35°C singularity (red dot), from which the clock returned to 35°C would be reset to a stochastic new phase. When $d_{25°C,35°C} = 0.1$, no trajectories take the clock to the 35°C singularity. When $d_{25°C,35°C} = 1$, every trajectory brings the clock to the 35°C singularity after certain period of time at 25°C, whose length is determined by where the trajectory starts on $LC_{35°C}$ (i.e. φ_{ini}). This is equivalent to the notion that for any 25°C pulse longer than a threshold value, there exists a corresponding φ_{ini} so that the pulse applied at it can take the clock to the 35°C singularity at the end of the pulse. When $d_{25°C,35°C} = 1.9$, only one trajectory passes through the 35°C singularity at a specific point, yielding one critical combination of φ_{ini} and τ that induces stochastic phases. **(B)** Heatmap showing how the possibility of triggering stochastic phases by a 25°C pulse at 35°C (quantified by $\Delta\varphi_{new}$ as illustrated in Fig. 20) depends on the pulse duration (τ) and where the 35°C singularity resides in relation to $LC_{25°C}$ (described by $d_{25°C,35°C}$, with $R_{25°C}$ set to 1). τ is scanned from 1 h to 30 h with 1 h step, and $d_{25°C,35°C}$ from 0.1 to 1.9 with 0.3 step.

h, yellow line), while a large $\Delta\varphi_{\mathrm{new}}$ suggests existence of stochastic phasing (e.g. Fig. 20, 12 h, yellow line). We presented the τ- and $d_{25°\mathrm{C},35°\mathrm{C}}$-dependent $\Delta\varphi_{\mathrm{new}}$ as a heatmap from blue (minimum level) to red (almost 360° spread in φ_{new} between synchronized cells) (Fig. 27B). For a small $d_{25°\mathrm{C},35°\mathrm{C}}$ where $\mathrm{LC}_{25°\mathrm{C}}$ encloses the 35°C singularity, the overall small, τ-independent $\Delta\varphi_{\mathrm{new}}$ (dark blue) indicates stochastic responses cannot be induced no matter how long the pulse is. Intuitively speaking, this is because no 25°C pulse can bring a clock state outside of $\mathrm{LC}_{25°\mathrm{C}}$ to the 35°C singularity that lies inside of it (Fig. 27A, left, dashed gray trajectories projecting from different phases along the red circle). As $d_{25°\mathrm{C},35°\mathrm{C}}$ approaches and rises slightly above $R_{25°\mathrm{C}}$ ($=1$), with the 35°C singularity lying on top or close to $\mathrm{LC}_{25°\mathrm{C}}$, the sharp transition from blue at $\tau = 11$ h to red at $\tau = 12$ h (indicated by the vertical black arrow at $d_{25°\mathrm{C},35°\mathrm{C}} = 1$ in Fig. 26B) indicates that a 25°C pulse longer than the threshold $\tau\sim11$ h, if applied at an appropriate φ_{ini}, can cause stochastic phasing (visualized in Fig. 27A, center; dark gray trajectories). If $d_{25°\mathrm{C},35°\mathrm{C}}$ is increased further, excluding the 35°C singularity from $\mathrm{LC}_{25°\mathrm{C}}$, the small range of τ in red (indicated by the two horizontal black arrows at $d_{25°\mathrm{C},35°\mathrm{C}} = 1.9$ in Fig. 27B) implies that only a particular length of pulse can induce stochastic new phases, as readily seen from the plot of clock-state trajectories in Fig. 27A (right; among dashed gray trajectories, one dark gray trajectory traversing red dot).

Chapter 3

Methods

3.1 Key resources table

REAGENT or RESOURCE	SOURCE	IDENTIFIER
Antibodies		
Rabbit polyclonal anti-KaiC serum	Rust et al., 2007 (made by Cocalico Biologicals)	N/A
Rabbit polyclonal anti-RpaA serum	Gutu and O'Shea, 2013 (made by Cocalico Biologicals)	N/A
Chemicals, Peptides, and Recombinant Proteins		
Phos-tag™ Acrylamide AAL-107	Wako Chemicals	Cat#304-93521
Experimental Models: Organisms/Strains		
S. elongatus Strain JRC35	Chabot et al., 2007	N/A
S. elongatus PCC 7942 (wild type)	ATCC	Cat#33912
Software and Algorithms		
Algorithm for phase retrieval	Waller et al., 2010	N/A
MATLAB® R2016a	MathWorks	https://www.mathworks.com/
ImageJ	National Institutes of Health	https://imagej.nih.gov/ij/
Deposited Data		
Raw microscopy data	This paper	https://www.dropbox.com/sh/3ibv70v5myx2nfg/AAA6sv2ZS8eOzwJqX5MOwuNXa?dl=0
MATLAB codes for microscopy data analysis		
Time course data of free-running oscillations at 25°C and 35°C, related to Fig. 15	This paper	http://dx.doi.org/10.17632/4pwgckvgjc.1
Dataset of extracted phase resetting responses		
Key MATLAB codes for model fitting and simulations		
Arduino codes for automatic entrainment device		
Other		
FoilCover for Lab-Tek II chambered coverglass	PeCon (ordered from Zeiss)	Cat#4107912012000000
RL1360 classic low power dark field ring light (white)	Advanced Illumination	Part#RL1360-WHI-C2

3.2 Experimental model and subject details

3.2.1 Cyanobacteria strain

Strain JRC35 (Chabot et al., 2007), which expresses the YFP-SsrA protein under the control of the *kaiBC* promoter and contains a kanamycin resistance cassette, was obtained from Alexander van Oudenaarden (Massachusetts Institute of Technology, currently at Hubrecht Institute).

3.2.2 Cell culture

Cells were grown in a shaking incubator (Innova 40, New Brunswick Scientific) in filtered BG-11 medium (components listed below) supplemented with 10 μg/mL kanamycin and 10 mM HEPES-NaOH Ph 7.5, and illuminated with cool-white fluorescent lights (two Phillips T9 circline bulbs – a 32 Watt, 12" diameter bulb encircling a 22 Watt, 8" diameter bulb). Growth temperature was set according to specific experiments (i.e. 25 °C, 30 °C, 35 °C, or 37.5 °C). BG-11 medium was sterile filtered to eliminate the precipitates formed after autoclaving, which affect imaging quality. Culture preparation for microscopy and western blotting time course experiments are described below in the method details section.

BG-11 medium components		Concentration (mg/L)
Milli-Q H_2O		N.A.
$NaNO_3$		1.5×10^3
K_2HPO_4		39
$MgSO_4\cdot7H_2O$		75
Na_2CO_3		20
$CaCl_2\cdot2H_2O$		35.8
EDTA		1
$FeNH_4$ citrate		12
Trace metal mix	H_3BO_3	2.86
	$MnCl_2\cdot4H_2O$	1.81
	$ZnSO_4\cdot7H_2O$	0.222
	$Na_2MoO_4\cdot2H_2O$	0.390
	$CuSO_4\cdot5H_2O$	0.079
	$Cu(NO_3)_2\cdot6H_2O$	0.049

3.3 Method details

3.3.1 Western blot analysis

Western blotting was performed following previously established procedures (Gutu and O'Shea, 2013; Rust et al., 2011) with modifications described below. Cells were collected by vacuum filtration on cellulous acetate filters (OE67, Whatman), placed into 500 μL screw-cap tubes containing 0.1 mm glass beads (BioSpec Products), flash-frozen in liquid nitrogen, and then stored at -80°C until lysis. Lysates were obtained by bead-beading at 4°C (6 times, 30 s each, with 1 min cooling on ice in between) in 250 μL ice-cold lysis buffer (7.5 M urea, 20 mM HEPES pH 8.0, 1 mM β-mercaptoethanol, and 1x cOmplete™ EDTA-free protease inhibitor tablet, Roche). The lysate was centrifuged for 10 min (16,000 x g, 4°C), after which the supernatant was transferred to a clean microcentrifuge tube. The total protein concentration of each sample was measured by the Bradford assay (Pierce) against a standard curve of bovine serum albumin (BSA, Bio-Rad) diluted in lysis buffer. For each SDS-PAGE gel, 12 μg of total protein lysate was loaded per lane.

To detect the phosphorylation level of KaiC, lysates were heated at 99°C for 3 min, loaded to a 10% Tris-HCl gel (acrylamide:bisacrylamide, 37.5:1, 16 cm×16 cm×1 mm), and then run at 35 mA and 15°C for ~7 h using a Hoefer™ SE600 electrophoresis system. After electrophoresis, the separated proteins were transferred to nitrocellulose membrane (0.45 μm pore size, Bio-Rad) at 100 mA for 90 min using the Trans-Blot SD semi-dry transfer cell (Bio-Rad), followed by standard Western blotting procedures. The membrane was incubated with primary antibody (1:1000 dilution of rabbit polyclonal anti-KaiC serum that was generated against full-length recombinant KaiC, Cocalico Biologicals) overnight at 4°C, and then with secondary antibody (1:1000 dilution of 10 μg/ml goat anti-rabbit HRP conjugate, Pierce) for 1 h at room temperature. The blot was

developed with SuperSignal West Femto maximum sensitivity substrate (Pierce), and imaged with an AlphaImager system (Alpha Innotech). KaiC was detected in multiple bands (see the data and software availability section for gel images) – the bottom two bands unambiguously correspond to unphosphorylated KaiC (U-KaiC), while the three phosphoforms (S-KaiC, T-KaiC, and ST-KaiC) cannot be clearly separated (Nishiwaki et al., 2004). Background-subtracted intensities of the multiple bands were quantified by densitometry using imageJ software (National Institutes of Health). The ratio of phosphorylated KaiC (KaiC~P%, Fig. 15) or unphosphorylated KaiC (1 - KaiC~P%) was determined by dividing the sum of the bottom two bands' (U-KaiC) by the sum of all bands' intensities.

To measure the phosphorylation level of RpaA, lysates were run at 4°C and 130 V on a 7% polyacrylamide gel (acrylamide: bisacrylamide, 29:1) containing 50 μM Phos-tag^{TM} Acrylamide AAL-107 (Wako Chemicals) and 100 μM $MnCl_2$, until the bromophenol blue dye reached the bottom of the gel in ~2 h. Before transferring the proteins to nitrocellulose membrane, the gel was gently washed twice for 10 min each time in transfer buffer (40 mM glycine, 50 mM Tris, 0.063% SDS, 20% v/v methanol), with 1 mM EDTA added to the first wash to chelate Mn^{2+} ions. Also, the primary antibody used was 1:1000 dilution of rabbit polyclonal anti-RpaA serum that was generated against full-length recombinant RpaA (Cocalico Biologicals). Except for these, other procedures were the same as those used in detecting KaiC. RpaA appears in two bands (see the data and software availability section for gel images) – the upper band is phosphorylated (RpaA~P), and the lower unphosphorylated (U-RpaA). Background-subtracted intensities of the two bands were quantified, and then normalized to their sum to calculate the ratio of phosphorylated RpaA (RpaA~P%, Fig. 15) or unphosphorylated RpaA (1 - RpaA~P%).

3.3.2 Time-lapse microscopy and analysis

Overview of experimental design

Single-cell phase resetting responses to temperature changes were measured with live cell imaging time courses. An imaging time course lasts 3-4 days, during which certain resetting signal was applied by changing the ambient temperature of imaged cells. Although cyanobacterial cells divide faster than 24 h (e.g. with a doubling time of ~12 h at 35°C and ~16 h at 25°C under our experimental conditions), because the clock runs independent of the cell cycle and its state is faithfully inherited at cell division (Yang et al., 2010), the dynamics of the clock-state reporter can be continuously traced across generations (Chabot et al., 2007; Mihalcescu et al., 2004; Teng et al., 2013; Yang et al., 2010), and the clock's phase before and after a signal can then be extracted. To increase the throughput of imaging, we loaded a mixed-phase population of cells for one imaging time course, so that a resetting signal applied during the time course was given to cells with different phases. Thus, summarizing the single-cell responses from one time course should theoretically suffice to generate the PTC of a given signal. When the pre-signal phases were, in reality, not uniformly sampled from 0° to 360° in a single time course experiment, the results from several experiments were combined to generate a PTC. Also, to avoid potential statistical bias due to variable sampling density of the pre-signal phases, we presented all results as single-cell data points.

Culture preparation for microscopy

700 μL per tube (BD Biosciences, 5ml polystyrene round-bottom tube) of liquid culture was inoculated at an initial OD_{750} of ~0.02, and grown with 140 rpm shaking to an OD_{750} between 0.2 and 0.4 before imaging. The incubator temperature was set to what cells should first experience in

the imaging time course they were prepared for (e.g. 37.5°C for the 37.5°C-to-25°C shift or 35°C for 25°C pulses in a 35°C background). To prepare stably oscillating cells with a given circadian phase, a tube of culture was entrained by at least two cycles of 12 h light/12 h darkness, and then released into constant light to free run for ~24 h, with a measured light intensity of ~15 μE m^{-2} s^{-1} maintained throughout the light periods. To obtain cells with a 360° spread of phases, we built an automatic device (Chabot et al., 2007) to simultaneously entrain twelve tubes of culture to different phases. The device comprises a platform that holds the tubes uniformly spaced around a circle (with 30° between two adjacent tubes), and, affixed to a programmed step motor, a half-circle shield that rotates 30° every 2 h, sequentially exposing each tube to cycles of 12 h light/12 h darkness (see the additional resources section for step motor tutorial, and the data and software availability section for detailed setup of the device).

Microscopy experimental setup

To set up one imaging time course, ~100 μL of cell culture was harvested from each of the twelve tubes. To guarantee equal sampling of cells with different phases, the exact volume of culture taken from each tube was adjusted to be inversely proportional to its OD_{750}. The mixture of these twelve tubes of cells (~1200 μL) was gently vortexed, concentrated by centrifuge, and then resuspended in 1 mL sterile-filtered BG-11 medium (without kanamycin). 5 μL of the resuspended cells were loaded onto the center of a Lab-Tek™ II chambered coverglass (Electron Microscopy Sciences), and overlaid by a pad of 1% agarose (2.5 cm×1.5 cm×6 mm). After a 3-4 days of the imaging time course, an individual cell in the first frame of image could grow into a colony of approximately 50~100 cells (Fig. 28A, D). To avoid crowding and overlapping of cells, the above

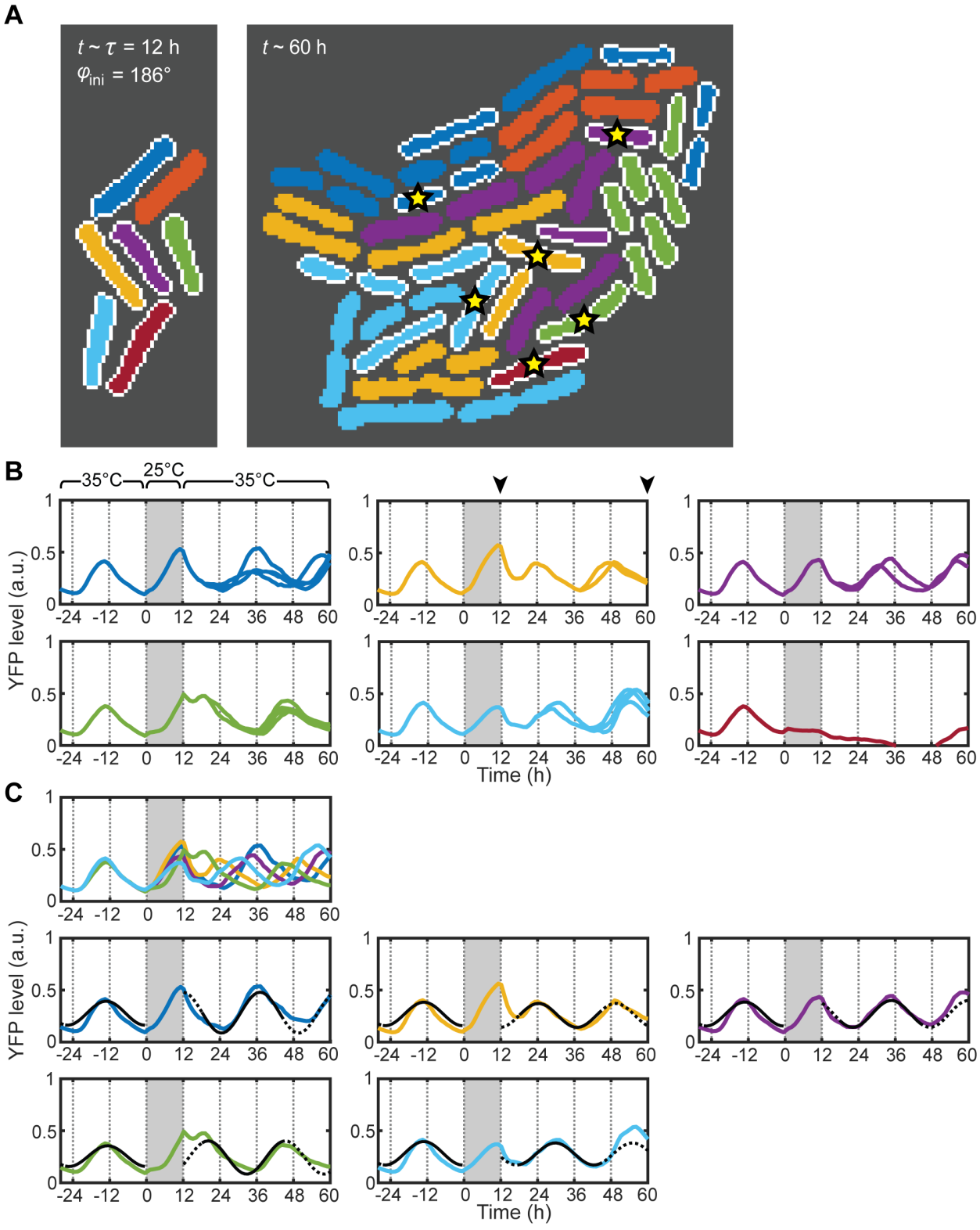
A
t ~ τ = 12 h
φini = 186°
t ~ 60 h
B
35°C
25°C
35°C
YFP level (a.u.)
Time (h)
C
YFP level (a.u.)
Time (h)

(Continued)

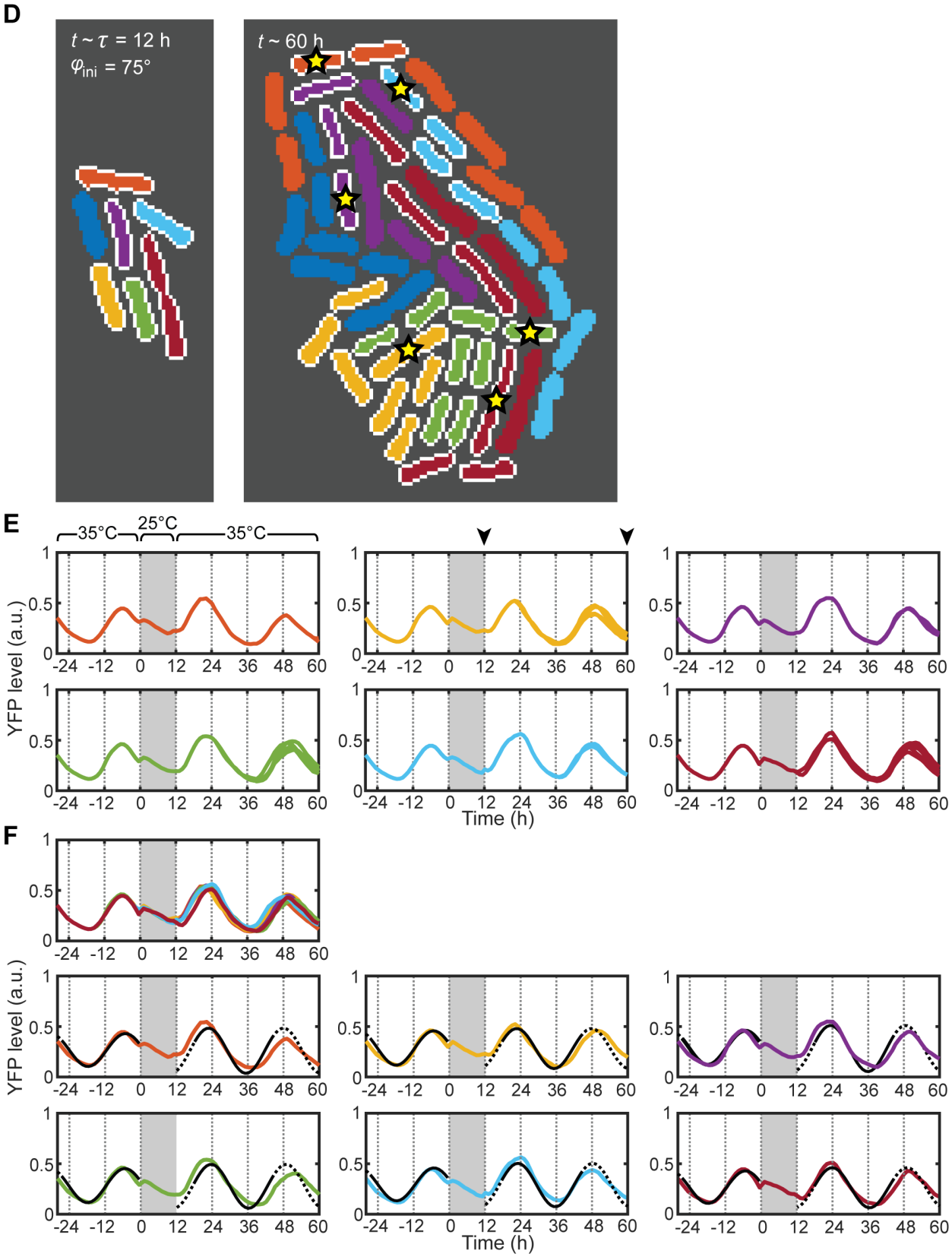
D
t ~ τ = 12 h
φini = 75°
t ~ 60 h
E
35°C
25°C
35°C
YFP level (a.u.)
Time (h)
F
YFP level (a.u.)
Time (h)

Figure 28 (Continued). Extracting steady-state phases from the YFP reporter dynamics. **(A) (B) (C)** and **(D) (E) (F)** display, in parallel, analysis of the two colonies of cells featured in the top vs. bottom panels in Fig. 6A. As **(A)**, **(B)**, **(C)** is each equivalent to **(D)**, **(E)**, **(F)**, only the first set are explained in detail. **(A)** Snapshots of automatically segmented cells at $t = 12$ h (at the end of the 25°C pulse, left) and at $t = 60$ h (48 h afterwards, right). Both time points are indicated by black arrows in **(B)**. Cells that can be automatically tracked throughout the time course (to $t = 60$ h) are outlined in white, and among them, the ones randomly chosen for quantifying phase resetting responses are labeled by a yellow star. Every segmented cell at $t = 60$ h, and if analyzed, its YFP reporter trace in **(B)** and **(C)** are color-coded to match the ancestor cell it was divided from at $t = 12$ h. **(B)** YFP reporter traces of all successfully tracked cells (white-outlined) in **(A)**, organized into different diagrams according to their ancestor cell at $t = 12$ h. The red trace in the bottom right diagram was removed from further analysis due to cell death. **(C)** Extracting phase information from the YFP reporter traces of selected cells (star-labeled) in **(A)**, shown altogether in the first diagram and then demonstrated one by one. In the single-trace diagrams, the solid black lines denote fitting the two intervals of a YFP reporter trace to cosine functions with the period $T_{35°\mathrm{C}} = 25.2$ h – from $t = -26$ h to $t = 0$ for defining φ_{ini}, and from $t = 18$ h to $t = 44$ h for extrapolating φ_{new}. The dashed black lines are extended from these cosine fits into other time intervals at 35°C.

culture volumes and agarose pad size were optimized to create a uniform sparse distribution of single cells to start with. To prevent the agarose pad from drying, the chambered coverglass was capped by a special foil cover (Pecon Products) that is permeable to air but not water, and a small drop of BG-11 medium (~100 μL) was placed at each end of the coverglass to increase the humidity inside the capped chamber. The foil has one hydrophobic and one hydrophilic side. To reduce moisture condensation on the foil which could form with a temperature drop (e.g. the 37.5°C-to-25°C shift), the foil was assembled with its hydrophobic side facing the sample (or interior of the chambered coverglass).

The sample was imaged with a Plan-Apochromat 100X/1.40 Oil Ph3 objective (Zeiss) in the Cell Observer system (Zeiss), equipped with Cascade II:512 camera (Photometrics) at 512×512 pixel resolution and a Lambda DG-4/DG-5 xenon arc lamp (Sutter Instrument) as the fluorescence source. Bright-field, YFP (Zeiss filter set 46 HE) and Cy3 (autofluorescence, Zeiss filter set 43

HE) images were taken at 16-20 designated positions every hour – at each position and time point, fluorescence images (YFP and Cy3) were taken in the best focal plane, and centered around it, bright-field images were acquired along a Z-stack of 9 planes with a step size of 0.2 μm. Definite Focus (Zeiss) was used to minimize the drift in Z-direction that may occur over time. Throughout the time course, the sample was illuminated at an intensity of ~8 μE m^{-2} s^{-1} by an external LED ring (Advanced Illumination), which was switched off only during image acquisition. The sample temperature was regulated by an InVivo Scientific incubator that encloses the entire microscope, and sequentially set to the values that constitute a temperature signal (e.g. 35°C then 25°C and then 35°C for the experiment of a 25°C pulse at 35°C). The incubator temperature is regulated by a built-in PID controller. Heating up the incubator (e.g. changing from 25°C to 35°C) takes ~30 min, while cooling it down (e.g. changing from 35°C to 25°C) would take much longer that that if depending solely on the PID controller. To speed up the cooling process also to ~30 min, the heater of the incubator was manually switched off until the temperature drops close to the target value, and the incubator doors were also opened during this process to help dissipate heat. Considering the timescale of the circadian period (~24 h) and the signals employed in our study (e.g. the shortest 25°C pulse was 3 h long), ~30 min is short enough for our needs; and we recorded the time at which a temperature signal was given by the starting point of this ~30 min stabilization process (i.e. the time of setting rather than reaching a new temperature). Also, since the foil cover could not completely seal the chamber in which the sample resides, to further prevent the sample from drying, several large beakers of water were placed inside the incubator to create a humidified environment around the chamber. Except for the incubator (whose temperature was manually adjusted), every other device involved was automated and coordinated by the MetaMorph software.

Image processing and data analysis

To extract the single-cell clock dynamics and their phase information, a custom written MATLAB software (R2016a, MathWorks) was developed following the standard steps of image processing and analysis (Chabot et al., 2007; Mihalcescu et al., 2004; Yang et al., 2010) (see the data and software availability section for raw images and codes). The software first segments individual cells in each frame using a quantitative phase map constructed from the z-stack bright-field images (Waller et al., 2010), and overlays the segmented cells with YFP and Cy3 images to deduct background fluorescence and extract the clock-state reporter level. It then tracks cells from one frame to another to construct their lineages and thereby generates time series of the reporter expression. The time series were then fitted by a cosine function (Markson et al., 2013; Refinetti et al., 2007) to quantify the pre- vs. post-resetting-signal phases as how they were defined in the main text (i.e. φ_{ini} vs. φ_{new} and φ_{bf} vs. φ_{af} respectively for temperature pulse and shift). As our study involves a substantial volume of time-lapse imaging data, to be more time efficient, we designed the analysis procedures to be as automated as possible. Specifically, we coded stringent standards in mapping cells between frames to guarantee the correctness of automatic lineage tracking results. Since the cell segmentation and tracking was performed using bright-field images, whether a lineage could be successfully tracked is independent of the phase resetting responses to be extracted from its YFP reporter trace. Therefore, although not all lineages were automatically trackable, we could use an unbiased subset of the tracked lineages to quantify single-cell responses (for randomly selecting a subset of tracked lineages, see section below, Determining the time windows to use for extracting phase information with an example 12 h 25°C pulse experiment).

On top of the standard image processing steps, two details need to be clarified. First, as the intensity of Xenon arc lamp decays over time and the lamp bulb has been changed twice throughout data acquisition, we couldn't well control excitation light intensity, and the absolute fluorescence level is not comparable among different time courses. This, however, does not affect building and constraining the model, since we used only the phase but not the amplitude information of single-cell YFP reporter traces. To plot the traces though (Fig. 6A, 9, 13, 28B, C, E, F), for illustrative purposes, we normalized the level of traces collected in different experiments so that the average peak YFP level at 35˚C stays the same. Second, Cy3 images were taken and analyzed first to examine the viability of imaged cells over time, and second to estimate and subtract the bleed-through from chlorophyll autofluorescence into the YFP channel, especially as the level of autofluorescence was observed to gradually increase through a time course. Regarding the first point, by the end of every single time course, ~1% cells formed aggregates foci in the Cy3 channel, indicative of cell stress or damage, and were excluded from further analysis. Regarding the second point, to assess and subtract the fraction of YFP fluorescence emitted from autofluorescence rather than the clock-state reporter, we imaged wild type cyanobacterial cells (containing no YFP reporter) over time at 35˚C to measure the ratio of its emission in the YFP channel to that in the Cy3 channel, and accordingly corrected the YFP images of the experimental strain (JRC35) using its Cy3 images (see the uploaded codes for details). Also, as with the time courses of phase resetting experiments, the wild type cells exhibited a slow steady increase in autofluoresncece over time, suggesting the increase is subject to our experimental conditions and not directly related to the responses to temperature changes.

Determining the time windows to use for extracting phase information with an example 12 h 25°C pulse experiment

To efficiently measure steady-state phase resetting responses, we need to determine the amount of time to image before and after a signal, and the time windows to use for extracting the pre- and post-signal phases. To quantify the pre-signal phase, only one full cycle of oscillations needs to be recorded. However, to avoid any transient fluctuations that might occur with transferring the cells from liquid culture to under the microscope, we can extend the imaging time by several hours and not use the first few time points of data. Following a temperature signal, it takes the clock a period of transient dynamics to establish stable oscillations. Thus, to quantify the steady-state phase shift to a signal, the longer we wait, the more likely the clock dynamics have stabilized. However, with a longer time course, it would be more difficult to maintain stable growth conditions and to generate high-quality data that are easy to process. Regarding the later point, large lateral drifts of the imaged positions tend to occur with long-term imaging (usually starting at 80~90 h); and automatic cell tracking is error-prone when cells become crowded after multiple days of growing and dividing. To balance the above opposing requirements and optimize the duration of a time course, we need to identify, after a signal, the immediate time window of stabilized YFP reporter dynamics that can be used to extract a clock's steady-state phase.

We tested the above considerations with a 12 h 25°C pulse experiment, and illustrate, in Fig. 28, results of the two colonies featured in Fig. 6A, B – Fig. 28A, B, C for the colony with $\varphi_{\mathrm{ini}}\sim186°$ at the onset of the pulse (top panel in Fig. 6A, blue dots in Fig. 6B), and an equivalent set of plots, Fig. 28D, E, F for the colony with $\varphi_{\mathrm{ini}}\sim75°$ at the pulse (bottom panel in Fig. 6A, red dots in Fig. 6B). Here, we will illustrate the analysis procedures using the first example colony where

stochastic phases were induced. In this test experiment, after pre-growing at 35°C and then being loaded under the microscope, cells were grown and imaged first at 35°C for ~28 h, then at 25°C for 12 h, and then again at 35°C for ~48 h. With the onset of the 12 h at 25°C pulse set to time 0, $t = -28$ h, $t = 12$ h and $t = 60$ h each corresponds to the beginning of the imaging time course, the end of the 25°C pulse, and the end of the time course. The colony was divided from a single cell at $t = -28$ h, the beginning of the time course. Through segmenting and tracking cells in this colony over time, from $t = -28$ h to $t = 60$ h, we obtained the YFP reporter traces of some individual cell lineages (Fig. 28B). Fig. 28A demonstrates the segmentation of cells in the first frame of image after the 25°C pulse at $t\sim12$ h (exactly at $t = 12.15$ h), and in the last frame of image at $t\sim60$ h (exactly $t = 60.15$ h). Cells were color-coded so that progeny at $t\sim60$ h retain the same color as their ancestor cell at $t\sim12$ h, and the ones belonging to tracked cell lineages were outlined in white. Fig. 28B shows, in matching color, their YFP reporter traces organized into different diagrams according to their corresponding (ancestor) cell at $t\sim12$ h. Occasionally, cells might die during a time course like the red cell in Fig. 28A (with its YFP reporter trace plotted in the bottom right diagram in Fig. 28B), and would be removed from further analysis. In the other five diagrams of Fig. 28B, the tracked lineages of each cell at $t\sim12$ h stay fairly synchronized for 48 h after the pulse, although the five progenies of cells are desynchronized from each other. This suggests that the stochastic new phase upon returning to 35°C is determined within a timescale shorter than the first cell division after the 25°C pulse, and stable oscillations persist afterwards. From all tracked lineages corresponding to certain cell at $t\sim12$ h in this colony, we then randomly selected one to quantify the steady-state phase resetting response as φ_{ini} vs. φ_{new} (Fig. 28C). In general, applying this selection method to all single colonies imaged in a time course ensured that, in response to a temperature signal (e.g. a 12 h 25°C pulse), all cells that experienced the last

change in temperature (e.g. shift from 25°C back to 35°C) were equally sampled, and their randomly picked individual lineages constituted an unbiased subset of data that could be used to generate the single-cell PTC of certain signal.

To extract the phase information of randomly selected lineages, we fitted their YFP reporter traces within the following time windows (Fig. 28C, solid black lines) to obtain φ_{ini} and φ_{new} (see Results and Fig. 5 for their definitions) – the last 26 h before the 25°C pulse (from $t = -26$ h to $t = 0$) was used to define φ_{ini} as the phase of the fitted cosine function at $t = 0$; and the first 26 h after 6 h following the 25°C pulse (from $t = 18$ h to $t = 44$ h) was used to extrapolate φ_{new} by what phase the fitted cosine function should start running from at $t = 0$. The period used to fit cosine functions should be the free-running period at 35°C, and was measured with a separate time course experiment (see section below, Measuring the free-running period at various temperatures). To evaluate whether the YFP reporter trace within the selected time window from $t = 18$ h to $t = 44$ h can represent stabilized oscillatory dynamics of the clock after the pulse, we extrapolated the fitted cosine functions (black lines) out to earlier and later times at 35°C (dashed black lines) to assist visual comparison of the fit with the data. Note the first 6 h right after the pulse – in the case (e.g. yellow and green traces) where the transient YFP reporter dynamics obviously differ from the extrapolated cosine function (dashed black lines from $t = 12$ h to $t = 18$ h), their difference diminishes within 6 h, suggesting fast establishment of the new phase as consistent with what was observed in Fig. 28B (i.e. the phase of a clock is determined within a timescale shorter than the first cell division after the 25°C pulse). The fact that the cosine functions extrapolated into later time (dashed black lines after $t = 44$ h) overlap with the YFP reporter traces as well as the prior fitted functions (black lines) confirms the new phase remains stable for at least two days after the

pulse. All the above features of the YFP reporter dynamics supports using the 6 h-to-32 h time window after a temperature change as an immediate period of stabilized YFP reporter dynamics to extract the clock's steady-state phase. To be consistent, in all phase resetting time course experiments, we imaged ~28 h before a temperature signal and at least 32 h afterwards, and used the last 26 h before the signal and the 6 h to 32 h after it to quantify steady-state responses (i.e. φ_{ini} vs. φ_{new} and φ_{bf} vs. φ_{af} respectively for temperature pulse and shift).

Examining the post-signal amplitude

As mentioned above, due to technical constraints (see the section on Image processing and data analysis), the absolute values of YFP fluorescence measurements cannot be used for rigorous, quantitative characterization of the phase resetting responses. Nevertheless, to qualitatively confirm that, in response to a critical perturbation, the circadian oscillations of individual cells persist afterwards, we examined their single-cell post-signal amplitudes and how they evolve over time following a signal. Specifically, for several example time courses imaged to 48 h after a temperature signal (the 12 h 25°C pulse experiment illustrated in the above section, and two time course experiments of the 25°C-to-35°C shift), we analyzed the post-signal YFP reporter oscillations within two different 26 h-long time windows after the end of the signal – an earlier 6 h-32 h window and a later 22 h-48 h window. As explained in the above section, the former was consistently used to extract the steady-state post-signal phases in all our experiments. The phase and amplitude during the earlier vs. later time windows are respectively denoted by φ and A, and φ' and A'. Comparing φ with φ' and A with A', we reached the following conclusions. 1) The PTCs generated using the post-signal phases extracted from the earlier vs. later time window (φ_{ini} vs. $\varphi_{\mathrm{new}}/\varphi'_{\mathrm{new}}$, or φ_{bf} vs. $\varphi_{\mathrm{af}}/\varphi'_{\mathrm{af}}$, blue vs. red circles; Fig. 8A, 12A, D) are similar and

overlapping. This supports the idea that there is rapid establishment of post-signal phases, which motivates using the earlier 6 h-32 h time window for quantifying steady-state phase shifts. 2) The amplitude during the earlier time window, A (Fig. 8B, 12B, E, blue triangles), varies with the pre-signal phase (i.e. φ_{ini} or φ_{bf}), and exhibits a reduction around the critical phase (indicated by dashed gray line) where stochastic post-signal phases are induced. In contrast, the amplitude during the later time window, A' (Fig. 8B, 12B, E, red triangles), is more uniform across different pre-signal phases; and for cells around the critical perturbations, those with obviously smaller amplitudes during the earlier time window (A; blue triangles circled out by yellow oval, Fig. 8B, 12B, E) have recovered their amplitudes during the later time window (A'; corresponding A vs. A' data points highlighted in yellow in Fig. 8C, 12C, F). These observations confirm that the circadian oscillations of individual cells persist following a phase resetting signal, and that cellular arrhythmicity could not be detected. However, some cells might still be stabilizing their oscillatory amplitudes during the earlier 6 h-32 h time window that was used to quantify steady-state post-signal phases; and specific to those around the critical perturbations, some would experience an obvious but transient reduction of the amplitude before recovering later.

Limitations and potential improvements of our current microscopy setup

As detailed in the above section, the slow recovery of oscillatory amplitude in some cells suggests that the 6 h-32 h time window used to extract φ_{new} and φ_{af} is, strictly speaking, an experimentally constrained approximation of stabilized post-signal oscillations. This approximation can largely capture the phase resetting responses as summarized by PTCs, including the critical-perturbation-induced stochastic phasing that manifests as a scattering in φ_{new} or φ_{af}. However, the quantitative distribution of stochastic post-signal phases might not be exact due to the challenges in accurately

determining the phases for cells with much reduced amplitude during the earlier 6 h-32 h time window. Nevertheless, this does not affect our basic theoretical interpretation that the unstable singularity underlies stochastic phasing, as the limit cycle model we used to arrive at this interpretation was constrained primarily by the deterministic phase resetting responses, and did not use the exact values of stochastic phases (see section of Limit-cycle model of the cyanobacterial circadian clock). That being said, monitoring the full relaxation processes in establishing steady-state phase resetting responses, and based on it, a refined characterization of the responses around critical perturbations are two unresolved remaining directions. Study of these issues necessitates maintaining good-quality imaging with homeostatic growth conditions for a longer duration – to at least 48 h after the end of a phase resetting signal.

3.3.3 Measuring the free-running period at various temperatures

For each temperature condition (i.e. 25°C, 30°C, 35°C or 37.5°C), the clock period was determined by cosinor fitting (Markson et al., 2013; Refinetti et al., 2007) the YFP reporter traces from a free-running time course. Specifically, cells were entrained and synchronized by two consecutive 12 h light/12 h darkness cycles – one in liquid culture and one under the microscope – before release into continuous light with bright-field, YFP, and Cy3 images taken for 48 h. Light/darkness conditions under the microscope were manually controlled by switching on or off the external LED ring; and during light periods, the LED intensity was kept constant at ~8 μE m^{-2} s^{-1}, the same as that in phase resetting experiments. The prior synchronization by light/darkness cycles was not necessary for identifying the period of free-running oscillations, but it could generate naturally well-aligned clock-state reporter traces of individual cells and facilitate visual inspection of the experimental data. With the onset of the 48 h time course set to $t = 0$, for all cell lineages (N >

700) that could be tracked throughout the time course (to $t = 48$ h), their YFP reporter traces from $t = 12$ h to $t = 48$ h were individually least square fitted to cosine curves with certain period. The period value was scanned from 24 h to 26 h with 0.1 h step, and determined by minimizing the sum of squared deviations between each trace and its cosine fit. The above analysis yielded the results of $T_{25°C} = 24.7$ h, $T_{30°C} = 25.0$ h, $T_{35°C} = 25.2$ h, $T_{37.5°C} = 24.9$ h, which were fixed at these values in quantifying the phases in phase resetting experiments.

We are aware that 25°C is near the lower temperature boundary for robust circadian oscillations, and thus confirmed that all cells imaged in the above free-running experiment at 25°C exhibit robust oscillations. Specifically, previous bioluminescence measurements at the population level have shown that since being released to continuous light (40~50 μE m^{-2} s^{-1}) after entrainment by light/darkness cycles, circadian oscillations start to damp after three days at 23°C (Xu et al., 2013) but persist at 25°C (Kondo et al., 1993). The lower temperature boundary for circadian oscillations must lie between 23°C and 25°C, while its exact value probably also depends on the other environmental conditions used (e.g. light intensity) (Xu et al., 2013). In our experiments of temperature shifts from 25°C (where cells were first grown and imaged at 25°C), the YFP reporter level of ~2% cells (which were excluded from analyzing phase resetting responses) appears arrhythmic for an initial or the whole (~28 h) period of time at 25°C. However, loss of robust oscillations was not observed during the 25°C periods in other phase resetting experiments (e.g. 25°C pulses at 35°C, temperature shifts towards 25°C), and also not in the above experiment of free-running oscillations at 25°C following a light/darkness cycle under the microscope. Thus, in all our imaging experiments, arrhythmicity at 25°C was only observed when cells were loaded under the microscope at 25°C and then immediately imaged afterwards. These observations

strongly indicate that circadian oscillations persist at 25°C, but they can be perturbed, at a low frequency, by transferring cells from liquid culture to under the microscope, which involves ~20 min of sample preparation at room temperature (18°C). Moreover, the fact that this phenomenon was not observed at any other temperatures (30°C, 35°C, or 37.5°C) suggests that the clock at 25°C is more susceptible to perturbations, consistent with the speculation that 25°C is near the lower boundary for robust oscillations.

3.3.4 Predicting the phase resetting by temperature shifts between 25°C and 35°C

A 25°C pulse at 35°C comprises two successive temperature shifts – first from 35°C to 25°C, and then from 25°C to 35°C. If the 25°C pulse (e.g. 24 h) is long enough to allow the stabilization of oscillatory dynamics at 25°C, these dynamics can be extrapolated to infer the steady-state responses to a 35°C-to-25°C shift. We thus predicted that the 35°C-to-25°C shift applied at all phases results in deterministic modulation of the circadian phase, which is suggested by the fact that, in response to a 24 h pulse applied across different φ_{ini}, the peaking time of the deterministic oscillations at 25°C is only slightly shifted comparing to previous oscillations at 35°C (Fig. 29, black lines). Moreover, for the clock that has stabilized its dynamics during a sufficiently long 25°C pulse, its responses to the 25°C-to-35°C shift later should be independent of any pre-25°C conditions it was experiencing. Therefore, for a clock free-running at 25°C, although it has not experienced the 35°C-to-25°C shift in the first place, the 25°C-to-35°C shift should also cause stochastic new phases, if it is applied when the YFP reporter of the clock at 25°C reaches near its peak. The above predictions were verified by experiments (Fig. 11).

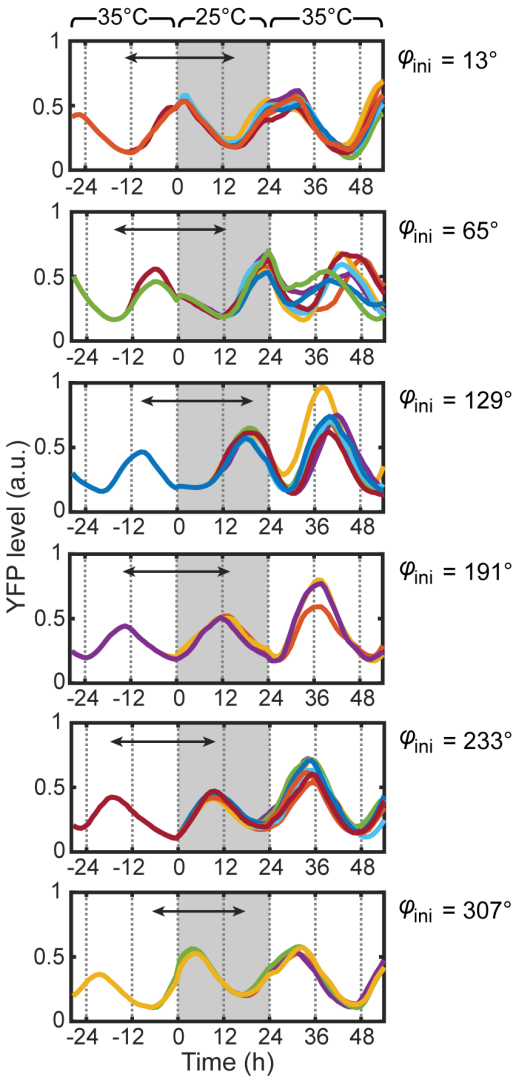

Figure 29. Shifting temperature from 35°C to 25°C is predicted to cause deterministic modulation of the circadian phase. YFP reporter traces exhibiting the phase resetting processes in response to a 24 h shift to 25°C applied at different phases at 35°C, with colonies of an average φ_{ini}~0°, 60°, 120°, 180°, 240°, and 300° shown as example. The black lines mark the time intervals between peaks (troughs) of the oscillations before and after the 35°C-to-25°C shift, which are ~24 h for all example φ_{ini} shown.

3.3.5 Limit-cycle model of the cyanobacterial circadian clock

The basic logic and structure of the model were laid out in the main text. Here we summarize the supporting details for developing the model (see the data and software availability section for model fitting and simulation codes), and delineate its implicit assumptions and caveats that need

to be considered before applying the model to other biological oscillators.

Dynamical structure of the cyanobacterial clock

The simplest and also most likely dynamical structure of the cyanobacterial clock consists of one unstable singularity (Fig. 30A, black dot at the center) residing inside a globally stable limit cycle (black circle). The reasoning is as follows: first, for a biological dynamical system, its stable steady

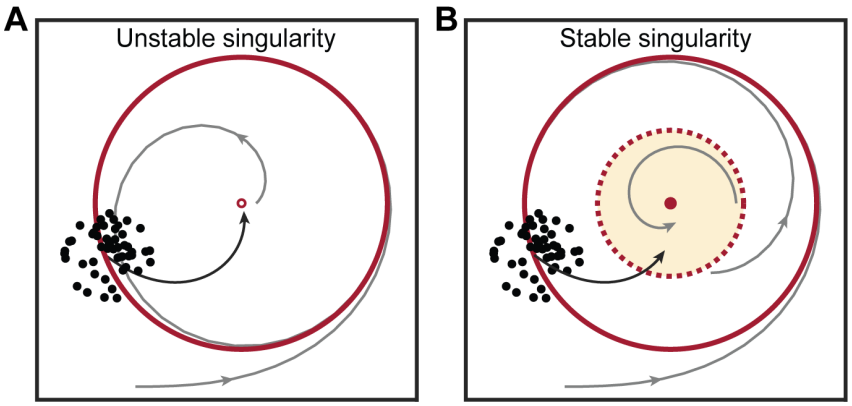

Figure 30. Schematics comparing cellular circadian clocks with a stable vs. unstable singularity. The singularity inside the stable limit cycle (solid red circle) characteristic of circadian oscillations can be **(A)** unstable (hollow red dot) or **(B)** stable (solid red dot). The gray trajectories indicate that **(A)** the stable limit cycle globally attracts any states other than the unstable singularity, and **(B)** the stable singularity and the stable limit cycle respectively attract states inside vs. outside the unstable limit cycle (dashed red circle). The black curve represents the critical perturbations that cause **(A)** stochastic phases or **(B)** arrhythmicity of individual clocks.

state or closed orbit should directly and respectively correspond to experimentally observable dynamical behavior – stable steady state to equilibrium, and stable closed orbit to oscillations. Since, under the conditions used in our study, the cyanobacterial clock exhibits only robust self-sustained circadian oscillations, their corresponding limit cycle should be the only stable solution of the clock system, and no other stable steady state or closed orbit should exist. Moreover, according to the Critical-point Criterion (simply put, a closed trajectory has a critical point in its

interior) (Strogatz, 2001), there should be at least one singularity (i.e. steady state) inside this stable limit cycle; and the singularity should be unstable since the clock system does not have stable steady states. Therefore, not considering any other unstable solutions (steady state or closed orbit) that theoretically could exist, the simplest dynamical structure of the cyanobacterial clock is a globally attractive limit cycle enclosing an unstable singularity. This scenario is also biologically most plausible, given the simple molecular network of the cyanobacterial clock (Rust et al., 2007). Lastly, it should be clarified that the dynamical structure of a system might vary with environmental conditions. For example, the cyanobacterial clock stops oscillating at 18°C (Xu et al., 2013), indicating that the stable limit cycle of circadian oscillations has collapsed into a stable steady state.

Dynamical structure of the mammalian clock

The same dynamical structure of a stable limit cycle enclosing an unstable singularity (Fig. 30B) can account for the critical-light-pulse-induced desynchronization among synthetically engineered mammalian cellular clocks in fibroblasts, which was reported by Pulivarthy et al. and Ukai et al. This phenomenon could be explained by the light pulse bringing the clock close to an unstable singularity at the end of the pulse. However, within this limit cycle framework, how can one reconcile the suppression of cellular rhythms (i.e. decrease of amplitude) observed by Pulivarthy et al.?

Specifically, Pulivarthy et al. observed that, concurrent with the induction of stochastic phases, the bioluminescence reporter of some cells displayed oscillations of very small amplitude or barely discernable oscillations for up to five days after a critical light pulse (traces in Fig. 5E of

(Pulivarthy et al., 2007). These cells could be either truly arrhythmic or exceedingly slow in stabilizing the oscillatory expression of the reporter. These two possibilities are difficult to differentiate due to the large fluctuations masking low-level bioluminescence expression. If the reporter is slow to stabilize, the following variation of the basic structure of a stable limit cycle enclosing an unstable singularity can qualitatively capture the experimental observations. First, as shown in Results (i.e. $t_1 \propto -\ln r_0$, if $r_0 \to 0$), in our current model based on the *Poincaré* oscillator, the stabilization of circadian oscillations could be slow if the clock happens to lie very close to the unstable singularity at the end of a critical light pulse. In such a case, in relaxing towards the limit cycle, the clock would spiral near the singularity for a long period of time; and during this period, the cellular noise might perturb the clock state across and diffuse it around the singularity, and further delay the stabilization of circadian rhythms. This scenario could apply to the mammalian cellular clock, since compared to the cyanobacterial clock, it has larger amplitude variation and phase drift even under constant free-running conditions and thus is intrinsically less robust and more prone to cellular noise. Second, the extended relaxation time could also be explained if the radial relaxation coefficient at a certain clock state (ε) positively correlates with its distance to the singularity (r) (Jewett et al., 1999) – so that the closer a clock is to the singularity, the longer it takes to relax back towards the limit cycle and to restore stable oscillations. Lastly, in the real multi-dimensional clock-state space where the limit cycle resides, more complex dynamical behavior might emerge around the unstable singularity (e.g. with both stable and unstable manifolds). This could give rise to different relaxation dynamics depending on how the clock is brought close to the unstable singularity by certain critical stimuli (Sun et al., 2016). In all the above scenarios, if a group of cellular clocks are brought close to the unstable singularity at the end of a critical light pulse, in addition to resulting stochastic phases, the clocks could also

display reduced oscillatory amplitudes for a prolonged period and larger cell-to-cell variation in the amplitudes during this period.

Alternatively, the dynamical structure of a stable singularity separated from a stable limit cycle by a minuscule unstable limit cycle surrounding the stable singularity (Fig. 30B) (Leloup and Goldbeter, 2001) could reconcile the seemingly differing findings of the two mammalian clock studies (Pulivarthy et al., 2007; Ukai et al., 2007). In such a case, the clocks brought to the interior of the minuscule unstable limit cycle (yellow region) would be attracted towards the stable singularity, resulting in damped small-amplitude oscillations. During this process, the clocks might also be perturbed by random noise to the outside of the minuscule unstable limit cycle (dashed circle), and then relax back into the stable limit cycle with stochastic phases. Compared to a stable limit cycle enclosing an unstable singularity, this explanation requires a more complicated dynamical structure and a strict constraint on the relative size of the unstable limit cycle. It is thus difficult to imagine that the mammalian clock network can satisfy all these proposed requirements, and we speculate that this scenario is less likely to hold true.

Dependence of oscillatory trajectories on temperature

As a system parameter of the clock, temperature was thought to affect the oscillatory trajectories (i.e. the limit cycle) of a free-running clock in our model (Fig. 16). To test this assumption, we measured, at both 25°C and 35°C, the circadian rhythms of a synchronized population in liquid culture by three clock outputs – the ratio of KaiC phosphorylation (KaiC~P%), the ratio of RpaA phosphorylation (RpaA~P%), and the average expression level of the YFP reporter (Fig. 15).

Although these measurements were not sufficient to fully delineate the differences between oscillatory trajectories at 25°C vs. 35°C, they did verify that temperature affects the trajectories.

To measure the circadian rhythms at either temperature, a ~350 mL culture of cells was entrained by two light/darkness cycles, released into constant light for 24 h, and then sampled every 2 h for 30 h. At every time point, 31 mL volume of cells were collected – two 15 mL aliquots were vacuum-filtered on cellulous acetate filters and frozen with liquid nitrogen for KaiC and RpaA immunoblotting, and 1 mL aliquot was concentrated by centrifugation and imaged immediately under the microscope. Images at every time point were analyzed like the individual frames in a time course (see the section of microscopy data analysis), and the average YFP reporter level (presented as mean ± standard deviation) was quantified using $N \sim 500$ cells. Throughout the entire course, the culture was grown in a tissue culture flask in the Innova 40 chamber and appropriately diluted to maintain an OD_{750} between 0.2 and 0.4. During light periods, it was shaken at 100 rpm, bubbled with CO_2-enriched air (1% v/v). In this experiment, the culture flask was placed closer to the fluorescent lights to reach a higher intensity of ~23 μE m^{-2} s^{-1}, and in a tilted position to obtain more uniform illumination. This intensity was adjusted to attain a similar growth rate (a doubling time of ~12 h at 35°C and ~16 h at 25°C) with the cells grown under an agarose pad. Although the light intensity at the culture flask was measured to be ~23 μE m^{-2} s^{-1}, the amount of light received by individual cells may be much lower than this value due to mutual cell shading in a large volume (~350 mL) of culture. In comparison, when pre-growing small volume (700 μL) of culture to prepare for imaging experiments, the measured ~15 μE m^{-2} s^{-1} intensity is probably closer to what individual cells in the culture were exposed to; and during imaging, the ~8 μE m^{-2} s^{-1} intensity at

the sample should well approximate what individual cells uniformly spread under an agarose pad were experiencing.

Deriving the noise-free PTC of temperature shift

To understand how the phase resetting by temperature shifts can be explained by modulation of the limit cycle geometry, we generically derived, not yet including noise, the PTC (i.e. φ_{bf} vs. φ_{af} relationship) of temperature shift from 1 to 2. See Results and Fig. 16 for the schematic setup of the following derivation. Given this setup, for a clock traversing certain state (Fig. 16, represented by yellow dot on the blue circle of LC_1) upon shifting temperature from 1 to 2, we first determined its φ_{bf} and φ_{af} according to how they were experimentally defined. As φ_{bf} is defined by the state of the clock at the time of temperature shift (Fig. 10, blue arrow), it should be the angular coordinate of the yellow-dot state in reference to LC_1 (Fig. 16). φ_{af} is extrapolated by tracing the stabilized post-shift rhythms (Fig. 10, dashed red line extended from red line) back to the time of the shift (red arrow). Thanks to the property of constant angular rotation that renders clocks running from any states along a radial axis eventually synchronized (e.g. gray and yellow dots in reference to LC_2 in Fig. 16), for the clock that relaxes towards LC_2 (red circle) from the yellow-dot state, tracing its stabilized rhythms (gray line that has spiraled into red circle) back (clockwise along LC_2) to the time of the shift would arrive at the gray dot and obtain φ_{af} as the same angular coordinate of the yellow and gray dots in reference to LC_2. With the model representation of φ_{bf} and φ_{af} determined, deriving the φ_{bf} vs. φ_{af} relationship becomes a simple geometry problem.

In a Cartesian frame centered at the temperature 1 singularity (Fig. 16, small blue circle) with the x-axis aligned to the 0° direction of LC_1, the yellow-dot state is located at $(R_1\cos\varphi_{\mathrm{bf}}, R_1\sin\varphi_{\mathrm{bf}})$,

and the temperature 2 singularity (red dot) is located at $\left(d_{1,2}\cos\alpha_{1-2}, d_{1,2}\sin\alpha_{1-2}\right)$. Thus, the vector from the temperature 2 singularity to the yellow-dot state is

$\vec{r} = \left(R_1\cos\varphi_{\mathrm{bf}} - d_{1,2}\cos\alpha_{1-2}\,, R_1\sin\varphi_{\mathrm{bf}} - d_{1,2}\sin\alpha_{1-2}\right)$.

In the same frame of reference, the unit vector of the 0° direction of LC_2 is

$\overrightarrow{r_0} = (-\cos(\alpha_{2-1} - \alpha_{1-2}), \sin(\alpha_{2-1} - \alpha_{1-2}))$.

Calculating φ_{af} as the directed angle from $\overrightarrow{r_0}$ to $\vec{r}$, we obtained φ_{af} as a function of φ_{bf}, with the parameters α_{1-2}, α_{2-1}, and the ratio $\frac{d_{1,2}}{R_1}$ (see Fig. 16 for their definitions).

If $\sin(\varphi_{\mathrm{bf}} + \alpha_{2-1} - \alpha_{1-2}) - \frac{d_{1,2}}{R_1}\sin\alpha_{2-1} \geq 0$,

$$\varphi_{\mathrm{af}} = 180° + \cos^{-1}\left(\frac{\cos(\varphi_{\mathrm{bf}}+\alpha_{2-1}-\alpha_{1-2}) - \frac{d_{1,2}}{R_1}\cos\alpha_{2-1}}{\sqrt{1+\left(\frac{d_{1,2}}{R_1}\right)^2 - 2\frac{d_{1,2}}{R_1}\cos(\varphi_{\mathrm{bf}}-\alpha_{1-2})}}\right), \text{ or else}$$

$$\varphi_{\mathrm{af}} = 180° - \cos^{-1}\left(\frac{\cos(\varphi_{\mathrm{bf}}+\alpha_{2-1}-\alpha_{1-2}) - \frac{d_{1,2}}{R_1}\cos\alpha_{2-1}}{\sqrt{1+\left(\frac{d_{1,2}}{R_1}\right)^2 - 2\frac{d_{1,2}}{R_1}\cos(\varphi_{\mathrm{bf}}-\alpha_{1-2})}}\right). \quad (1)$$

This function holds except for one case where LC_1 (blue circle) passes through the temperature 2 singularity (red dot) ($d_{1,2} = R_1$) at the state $(R_1\cos\alpha_{1-2}\,, R_1\sin\alpha_{1-2})$, and the clock traverses this state at the time of temperature shift ($\varphi_{\mathrm{bf}} = \alpha_{1-2}$). In this case, the clock lies right on its singularity upon being transferred to temperature 2, and φ_{af} is accordingly undefined. In reality, with the existence of noise that randomly perturbs the clock state off the singularity, it will relax into LC_2 with an unpredictable phase.

Plotting the above function with φ_{bf} and φ_{af} respectively as the x- and y-axis gives the noise-free PTC. Qualitatively speaking, the values of α_{1-2} and α_{2-1} determine the position (i.e. x- and y-

intercepts) of the curve, while the ratio $\frac{d_{1,2}}{R_1}$ influences its shape as exemplified with the following limiting cases. When $\frac{d_{1,2}}{R_1} \to 0$ signifying a minuscule shift of the singularity by temperature, $\varphi_{\mathrm{af}} = \varphi_{\mathrm{bf}} + \alpha_{2-1} - \alpha_{1-2} + 180°$, and the φ_{bf} vs. φ_{af} curve becomes a line with slope 1. When $\frac{d_{1,2}}{R_1} = 1$ which indicates that LC_1 passes through temperature 2 singularity, except for at $\varphi_{\mathrm{bf}} = \alpha_{1-2}$ where φ_{af} is undefined, $\varphi_{\mathrm{af}} = \frac{1}{2}\varphi_{\mathrm{bf}} + \alpha_{2-1} - \frac{1}{2}\alpha_{1-2} + 90°$, which is a line with slope 0.5. When $\frac{d_{1,2}}{R_1} \to \infty$ approximating a large shift of the singularity, $\varphi_{\mathrm{af}} = \alpha_{2-1}$ as a constant.

Interchanging the subscripts 1 and 2 in the above function, we immediately obtained the φ_{bf} vs. φ_{af} relationship of temperature shift from 2 to 1, which depends on the parameters α_{1-2}, α_{2-1}, and the ratio $\frac{d_{1,2}}{R_2}$.

If $\sin(\varphi_{\mathrm{bf}} + \alpha_{1-2} - \alpha_{2-1}) - \frac{d_{1,2}}{R_2}\sin\alpha_{1-2} \geq 0$,

$$\varphi_{\mathrm{af}} = 180° + \cos^{-1}\left(\frac{\cos(\varphi_{\mathrm{bf}}+\alpha_{1-2}-\alpha_{2-1}) - \frac{d_{1,2}}{R_2}\cos\alpha_{1-2}}{\sqrt{1+\left(\frac{d_{1,2}}{R_2}\right)^2 - 2\frac{d_{1,2}}{R_2}\cos(\varphi_{\mathrm{bf}}-\alpha_{2-1})}}\right), \text{ or else}$$

$$\varphi_{\mathrm{af}} = 180° - \cos^{-1}\left(\frac{\cos(\varphi_{\mathrm{bf}}+\alpha_{1-2}-\alpha_{2-1}) - \frac{d_{1,2}}{R_2}\cos\alpha_{1-2}}{\sqrt{1+\left(\frac{d_{1,2}}{R_2}\right)^2 - 2\frac{d_{1,2}}{R_2}\cos(\varphi_{\mathrm{bf}}-\alpha_{2-1})}}\right). \quad (2)$$

<u>Simulating single-cell responses to temperature shifts</u>

Before delving into the simulation procedures, it should first be clarified that our model is fundamentally deterministic. To account for the variation in phase resetting responses among

approximately synchronized cells, we added a noise term (see Results and Fig. 14 for details) to simulate cellular clock states. However, we did not investigate what factors contribute to cellular noise, which requires stochastic modeling. We focused instead on how phase resetting processes, that can be approximated as deterministic, drive a similar degree of noise in clock state towards different consequences – stochastic vs. deterministic phases. We did not closely look into the noise term with our conceptual model because it is unclear how the distribution of two-dimensional state points biophysically correlates with variation in the steady-state phases extrapolated from the YFP reporter. Future mechanistic studies might enable a meaningful inspection of the noise term, but it requires comprehensive molecular measurements and clock-network-based simulations that are directly comparable with each other.

Given the above rationale of the model, simulations of single-cell responses to temperature shift from 1 to 2 (Fig. 16), for example, were performed using the MATLAB software (R2016a, MathWorks) in following procedures.

0) The random displacement to a clock state at temperature 1 (before the shift), $(\Delta x_{\mathrm{bf}}, \Delta y_{\mathrm{bf}})$, is generated to be uniformly distributed within a disk of radius $k \cdot R_1$, and that at temperature 2 (after the shift), $(\Delta x_{\mathrm{af}}, \Delta y_{\mathrm{af}})$, within a disk of radius $k \cdot R_2$ (see section below for determining parameter values). Also, the term 'LC_1 (or LC_2) frame' denotes the Cartesian frame centered at temperature 1 (2) singularity with the x-axis aligned to the 0° direction of LC_1 (LC_2).
1) In LC_1 frame, to a clock that, if without noise, traverses the state $\left(R_1 \cos \varphi_{\mathrm{bf}}^0, R_1 \sin \varphi_{\mathrm{bf}}^0\right)$ at the time of temperature shift, we added $(\Delta x_{\mathrm{bf}}, \Delta y_{\mathrm{bf}})$ to simulate the clock state as $\left(R_1 \cos \varphi_{\mathrm{bf}}^0 + \Delta x_{\mathrm{bf}}, R_1 \sin \varphi_{\mathrm{bf}}^0 + \Delta y_{\mathrm{bf}}\right)$ at the time of the shift (Fig. 19, blue dots), and computed φ_{bf} as the angular coordinate of the clock state in LC_1 frame.

2) After the temperature shift, the clock spirals into LC_2 (Fig. 19B; gray line spiraling into red circle). Not yet considering noise, the after-shift phase $\varphi_{\mathrm{af}}^{0}$ is the angular coordinate of the above clock state in reference to LC_2, and was computed as the angle from the 0° direction of LC_2, $\overrightarrow{r_0} = (\cos(\alpha_{2-1} - \alpha_{1-2}), \sin(\alpha_{2-1} - \alpha_{1-2}))$, to the clock-state vector $\vec{r} = \left(R_1 \cos\varphi_{\mathrm{bf}}^{0} + \Delta x_{\mathrm{bf}} - d_{1,2}\cos\alpha_{1-2}, R_1 \sin\varphi_{\mathrm{bf}}^{0} + \Delta y_{\mathrm{bf}} - d_{1,2}\sin\alpha_{1-2}\right)$.
3) Transforming to LC_2 frame, to incorporate noise at temperature 2, we added $(\Delta x_{\mathrm{af}}, \Delta y_{\mathrm{af}})$ to the noise-free state $\left(R_2\cos\varphi_{\mathrm{af}}^{0}, R_2\sin\varphi_{\mathrm{af}}^{0}\right)$ extrapolated from tracing the stabilized rhythms at temperature 2 back to the time of the shift, and computed φ_{af} as the angular coordinate of the state point $\left(R_2\cos\varphi_{\mathrm{af}}^{0} + \Delta x_{\mathrm{af}}, R_2\sin\varphi_{\mathrm{af}}^{0} + \Delta y_{\mathrm{af}}\right)$ in LC_2 frame. The above state equivalently represents where the clock can possibly arrive after one free-running period (T) of time since being transferred to temperature 2 (Fig. 19, orange dots).

To scan the circadian phase at which the temperature shift was applied, we varied φ_1 from 0° to 360° with 1° step, and sampled n times around each φ_1 – for clear illustration, we chose $n = 20$ in simulating the single-cell PTCs (Fig. 18, 24), and $n = 50$ in plotting the limit cycle diagrams (Fig. 19).

As detailed above and also in simulating the responses to 25°C pulses later, although fluctuations exist throughout the entire phase resetting process, we summarized and approximated the influence of noise by perturbing the clock states upon shifts of temperature in a stepwise manner. This simplified approach suffices for the goal and nature of our model as clarified beforehand; and we will leave exact stochastic simulations like the Gillespie algorithm (Teng et al., 2013) to future mechanistic studies. Also, as in analytic derivation, simulating the steady-state responses to temperature shifts do not require modeling the relaxation dynamics of the clock system. The gray

relaxation trajectory in Fig. 19B was shown purely for illustrative purposes, and was computed with the relaxation coefficient ε constrained by fitting phase resetting responses to temperature pulses.

Recapitulating the phase resetting responses to temperature shifts between 25°C, and 30°C, 35°C, 37.5°C respectively

Recapitulating the phase resetting responses to shifts between two temperatures – still generically referred to as 1 and 2 – requires optimizing the six parameters R_1, R_2, $d_{1,2}$, α_{1-2}, α_{2-1}, and k. Not yet considering the occasionally induced stochastic responses exhibited as a scattering of φ_{af} around a particular φ_{bf} (e.g. in shifting temperature from 25°C to 35°C at $\varphi_{\mathrm{bf}}\sim 0°$; Fig. 18A), the typically deterministic responses display a tight distribution of single-cell φ_{bf} vs. φ_{af} data points along a clear trend line (Fig. 18, 24). The limit cycle geometry parameters (R_1, R_2, $d_{1,2}$, α_{1-2}, and α_{2-1}) determine the shape and position of a noise-free PTC, which should approximate the trend line in a good fit to data. As explained before (see the section of deriving the noise-free PTC of temperature shift), the ratio $\frac{d_{1,2}}{R_1}$ or $\frac{d_{1,2}}{R_2}$ respectively regulates the shape of the PTC of temperature 1-to-2 or 2-to-1 shift, while the values of α_{2-1} and α_{2-1} influence the position of the PTC in shifts of both directions. Thus, we could estimate the values of $\frac{d_{1,2}}{R_1}$, $\frac{d_{1,2}}{R_2}$, α_{2-1} and α_{2-1} by minimizing the least square differences between the noise-free PTCs derived from functions (1) and (2) and the single-cell data points of the deterministic responses to temperature shifts in both directions. The parameter k captures the natural degree of cell-to-cell variation displayed in deterministic phase resetting responses, and was tuned to reproduce the spread of single-cell data points along a trend line. In the case where stochastic responses were also observed (e.g. in the shifts between

25°C to 35°C), we confirmed whether simulations using the parameter values estimated purely from deterministic responses can reproduce the induction of stochastic phases (and they do), and if necessary, slightly adjusted the values to guarantee quantitatively capturing the single-cell data point distribution across the full range of sampled φ_{bf}.

The above procedures summarize how we recapitulated the responses to shifts between the three pairs of temperatures studied, i.e. 25°C, and 30°C, 35°C, or 37.5°C respectively. There are two additional details of our parameter choice. First, the three size-related parameters, R_1, R_2, and $d_{1,2}$, enter the functions (1) and (2) as two ratios, $\frac{d_{1,2}}{R_1}$ and $\frac{d_{1,2}}{R_2}$. This means that the limit cycle geometry holds only in relative terms, and that practically, we can set one limit cycle as a unit circle (e.g. set $R_1 = 1$), and scale and position the other accordingly (e.g. adjust the values of R_2 and $d_{1,2}$). Since 25°C is involved in each of the three pairs of temperatures, we set $R_{25°\mathrm{C}} = 1$ for convenience. Also, since we assumed the noise in clock state (Fig. 14, radius of gray-dot disk) at any temperature to be proportional to the radius of its corresponding limit cycle, k which denotes this proportion is temperature independent and technically, should be set by fitting the data of all temperature shifts together. However, as in conducting this research, we studied the responses to shifts between 25°C and 35°C earlier, the value of k was constrained from these data and then kept fixed.

All parameter values obtained are summarized in Table. 1 and graphically represented in Fig. 14 showing $k = 0.3$ and in Fig. 17, 25, 26 illustrating the relative limit cycle geometry. The phase resetting responses modeled using these parameter values is presented in Fig. 18 and 24, with black lines indicating the noise-free PTCs generated from functions (1) and (2), and red dots representing the single-cell simulations. Two points need to be clarified. First, the value of $R_{30°\mathrm{C}}$ (starred in

Table 1) cannot be well constrained. It should be derived from fitting the experimental data of the 30°C-to-25°C shift (Fig. 24A, right), which is tightly distributed along a slope 1 line indicative of a small ratio of $\frac{d_{25°C,30°C}}{R_{30°C}}$ and thus large value of $R_{30°C}$ (note in the section of deriving the noise-free PTC of temperature shift that, in the limiting case of $\frac{d_{1,2}}{R_1} \to 0$, $\varphi_{\mathrm{af}} = \varphi_{\mathrm{bf}} + \alpha_{2-1} - \alpha_{1-2} + 180°$, which is a line of slope 1), but the goodness of fit monotonically improves with decreasing $\frac{d_{25°C,30°C}}{R_{30°C}}$ towards 0 (i.e. increasing $R_{30°C}$ towards infinity). However, $R_{30°C}$ cannot be infinity in reality, so we arbitrarily set it to the value of $R_{35°C}$. This, however, does not affect our ability to infer the position of the 30°C singularity with respect to $LC_{25°C}$, which is determined by the ratio of $\frac{d_{25°C,30°C}}{R_{25°C}}$ that can be constrained from the responses to temperature shift in the other direction – from 25°C to 30°C (Fig. 24A, left). Also, we plotted all limit cycles together in one diagram (Fig. 25) to assist comparing the relative geometry between $LC_{25°C}$, and $LC_{30°C}$, $LC_{35°C}$, or $LC_{37.5°C}$ respectively. However, the geometric relationship that $LC_{30°C}$, $LC_{35°C}$, and $LC_{37.5°C}$ appear to have in this diagram is not necessarily meaningful. Fundamentally, it remains to be tested whether our two-dimensional limit cycle framework can simultaneously model the clock dynamics at more than two temperatures. The last section of considerations for broadly applying our model provides a detailed discussion on this issue.

Recapitulating the phase resetting responses to 25˚C pulses at 35˚C

To recapitulate the responses to 25˚C pulses at 35˚C with the *Poincaré* oscillator (see Results for equations) that was used to approximate the clock dynamics, only one more parameter – the relaxation coefficient ε – can vary and be optimized. As with the experiments of temperature shifts, if not considering the stochastic phases induced by multiple critical perturbations, the

typically deterministic responses to various lengths of 25˚C pulses (3 h, 6 h, … 24 h) exhibit a tight distribution of φ_{ini} vs. φ_{new} data points along clear trend lines in the single-cell PTC plots (Fig. 7). Given certain value of ε, we can deterministically simulate the temporal evolution of the clock system and compute a φ_{ini} vs. φ_{new} curve for each measured length of 25˚C pulse, which should approximate the PTC trend line in a good fit to data. Therefore, using the least square method, we optimized the value of ε to 0.32 h^{-1} (Table 1) by fitting the simulated φ_{ini} vs. φ_{new} curves (Fig. 20, black curves) of all 25˚C pulses to their corresponding single-cell data of deterministic phase resetting responses.

Table 1. Model fitting and simulation parameters. See Methods for deriving the parameter values below, and Results and Fig. 16 for the definitions of limit cycle geometry parameters. $R_{30°\mathrm{C}}$ is starred (*) to indicate that its value cannot be well constrained and was arbitrarily chosen (see Methods).

Limit cycle topology		$R_{25°\mathrm{C}}$	1		
Between 25°C and 30°C		Between 25°C and 35°C		Between 25°C and 37.5°C	
$R_{30°\mathrm{C}}$ *	3.92	$R_{35°\mathrm{C}}$	3.92	$R_{37.5°\mathrm{C}}$	1.96
$d_{25°\mathrm{C},30°\mathrm{C}}$	0.82	$d_{25°\mathrm{C},35°\mathrm{C}}$	1.18	$d_{25°\mathrm{C},37.5°\mathrm{C}}$	1.54
$\alpha_{25°\mathrm{C}-30°\mathrm{C}}$	20°	$\alpha_{25°\mathrm{C}-35°\mathrm{C}}$	5°	$\alpha_{25°\mathrm{C}-37.5°\mathrm{C}}$	340°
$\alpha_{30°\mathrm{C}-25°\mathrm{C}}$	205°	$\alpha_{35°\mathrm{C}-25°\mathrm{C}}$	199°	$\alpha_{37.5°\mathrm{C}-25°\mathrm{C}}$	172°
Degree of noise		k	0.3		
Relaxation coefficient		ε	0.32 h^{-1}		

Specifically, if denoting a certain length of 25°C pulse applied at a particular initial phase as (τ, φ_{ini}), the multiple critical perturbations experimentally observed to cause stochastic phases are (12 h, ~186˚), (15 h, ~166˚), (18 h, ~122˚), (21 h, ~83˚), and (24 h, ~55˚) (Fig. 7). Thus, in estimating the value of ε, among the single-cell φ_{ini} vs. φ_{new} data points of 12 h to 24 h pulses,

we did not include the more scattered points that fall within a 40˚-wide window centered at the above φ_{ini} values, which were defined by where the single-cell PTCs display maximum ~360˚ spread in φ_{new}. To test whether the model constrained from deterministic phase resetting responses can coherently account for the stochastic responses to the critical perturbations, we then performed single-cell simulations with the noise term added (Fig. 20, red points), and confirmed this by reproducing the spread of the single-cell data points that were not used to optimize ε.

To compute the φ_{ini} vs. φ_{new} relationship of certain length (τ) of 25˚C pulse at 35˚C, we first used the MATLAB's standard solver for ordinary differential equations (ODEs), ode45, to numerically simulate the trajectory the clock takes in traveling between $LC_{25°C}$ and $LC_{35°C}$ throughout a pulse signal (Fig. 22; gray lines), with the dynamics at either temperature governed by the *Poincaré* oscillator equations, and the relative geometry between $LC_{25°C}$ and $LC_{35°C}$ set as earlier (Table 1). Since the *Poincaré* oscillator has analytic solutions (see Results), rather than using the ode45 function for numerical simulations, we could derive the clock state as a function of time, and then specify the values of τ and ε to obtain its trajectory. This method is however much more complicated and thus not adopted. After simulating the clock-state trajectory, we then quantified the values of φ_{ini} and φ_{new} according to how they were experimentally defined (Fig. 5), which is illustrated here with the example of a 12 h pulse applied at $\varphi_{\mathrm{ini}} = 120^{\circ}$ in Fig. 22A. φ_{ini} is characterized by the clock state at the onset of the pulse (Fig. 5, blue arrow), and corresponds to the angular coordinate of this state with respect to $LC_{35°C}$ (Fig. 22A, left). φ_{new} is referenced to the same time, but as the extrapolated state derived from tracing the stabilized rhythms after the pulse back to the onset of it (Fig. 5, red arrow). If tracing the rhythms back to the end of the pulse instead, thanks to the property of constant angular rotation of the clock in our model, the

extrapolated phase, as denoted by φ'_{new}, should correlate to the angular coordinate of the end-of-pulse clock state in reference to $\mathrm{LC}_{35^{\circ}\mathrm{C}}$ (Fig. 22A, middle). The reasoning is identical to that detailed in quantifying φ_{af} in response to a temperature shift (see section above, Deriving the noise-free PTC of temperature shift). Tracing the rhythms further back from the end to the onset of the pulse, we thus arrived at $\varphi_{\mathrm{new}} = \varphi'_{\mathrm{new}} - \frac{360^{\circ}\tau}{T_{35^{\circ}\mathrm{C}}}$. Note that in our model, to derive φ_{new} requires simulating the transient clock-state trajectory during the 25˚C pulse but not that afterwards at 35˚C. It also implies that the relaxation coefficient ε was estimated only from the clock dynamics at 25˚C. For illustrative purposes, though, we still simulated and plotted how the clock relaxes back into $\mathrm{LC}_{35^{\circ}\mathrm{C}}$ using the same value of ε (Fig. 22A, B, right; gray line).

To simulate the single-cell responses to 25˚C pulses, we tracked the temporal evolution of the clock system throughout the different stages constituting a pulse signal (i.e. first at 35˚C, and then 25˚C, and then back to 35˚C), and at each stage, introduced noise by adding a random displacement to the deterministically computed clock state. This approach is consistent with how we simulated the responses to temperature shifts. The specific steps are as follows.

0) The random displacement to a clock state at 25˚C (or 35˚C) is uniformly distributed within a disk of radius $k \cdot R_{25^{\circ}\mathrm{C}}$ (or $k \cdot R_{35^{\circ}\mathrm{C}}$). Also, all following coordinates are referenced to the 35˚C singularity, and angles to the 0˚ direction of $\mathrm{LC}_{35^{\circ}\mathrm{C}}$ (Fig. 22A, B, left; red line).
1) To a clock at 35˚C that, if without noise, traverses the state $(R_{35^{\circ}\mathrm{C}}\cos\varphi^0_{\mathrm{ini}}, R_{35^{\circ}\mathrm{C}}\sin\varphi^0_{\mathrm{ini}})$ upon being transferred to 25˚C, we added the random displacement $(\Delta x_{\mathrm{ini}}, \Delta y_{\mathrm{ini}})$ to simulate the clock state as $(R_{35^{\circ}\mathrm{C}}\cos\varphi^0_{\mathrm{ini}} + \Delta x_{\mathrm{ini}}, R_{35^{\circ}\mathrm{C}}\sin\varphi^0_{\mathrm{ini}} + \Delta y_{\mathrm{ini}})$ at the onset of the pulse (Fig. 22A, B, left; black dots), and computed φ_{ini} as the angular coordinate of this clock state.

2) This initial state was then evolved using the *Poincaré* oscillator equations, to derive where the clock arrives after relaxing towards $LC_{25^\circ C}$ for a period of τ, as denoted by $\left(x^0_{\mathrm{eop}}, y^0_{\mathrm{eop}}\right)$ with 'eop' stranding for 'end-of-pulse'. To account for the noise at 25˚C, we added the displacement $\left(\Delta x_{\mathrm{eop}}, \Delta y_{\mathrm{eop}}\right)$ to approximate the actual end-of-pulse clock state as $\left(x^0_{\mathrm{eop}} + \Delta x_{\mathrm{eop}}, y^0_{\mathrm{eop}} + \Delta y_{\mathrm{eop}}\right)$ (Fig. 22A, B, middle; black dots), and calculated its angular coordinate φ_{eop}.
3) The clock returned to 35˚C would relax back into $LC_{35^\circ C}$, and stabilize its oscillatory trajectory following a period of transient dynamics (Fig. 22A, B, right; gray line spiraling into red circle). If not considering the noise back at 35˚C, φ_{eop} is exactly the φ'_{new} as defined above. To include the effects of noise though, we added another random displacement $(\Delta x_{\mathrm{new}}, \Delta y_{\mathrm{new}})$ to the state $\left(R_{35^\circ C}\cos\varphi_{\mathrm{eop}}, R_{35^\circ C}\sin\varphi_{\mathrm{eop}}\right)$ that was extrapolated from tracing the stabilized trajectory back to the onset of 35˚C (or end of the 25˚C pulse); and then computed φ'_{new} as the angular coordinate of the state $\left(R_{35^\circ C}\cos\varphi_{\mathrm{eop}} + \Delta x_{\mathrm{new}}, R_{35^\circ C}\sin\varphi_{\mathrm{eop}} + \Delta y_{\mathrm{new}}\right)$, and derived φ_{new} as $\varphi'_{\mathrm{new}} - \frac{360^\circ\tau}{T_{35^\circ C}}$. The above noise-added state equivalently represents where the clock can possibly arrive after running for a period of $T_{35^\circ C}$ since returned to 35˚C (Fig. 22A, B, right; black dots).

<u>Considerations for broadly applying our model</u>

To extend our model to a broader type and range of resetting signals or to other oscillatory systems, there are several considerations regarding how to simulate the dynamics of a system. First, the limit cycle of a free-running clock is typically determined by its current conditions, while in some rare cases, it depends also on the previous conditions the clock was experiencing. For example, due to the light-dependent circadian regulation of KaiABC stoichiometry, the asymptotic

trajectories (i.e. limit cycle) in darkness depend also on the phase of the clock at the transition from light to darkness (Hosokawa et al., 2013).

The second point concerns the validity of the assumptions we made to simplify the model. With an appropriate homeomorphic transformation, we can map the multi-dimensional clock-state space onto a two-dimensional plane, so that the limit cycle at a given temperature forms a circle centered at its corresponding singularity, and the clock spirals into or along it with a constant angular velocity (Fig. 14). However, when modeling several distinct temperatures together, it is not guaranteed that there exists a transformation that, in mapping clock states onto a two-dimensional plane, can simultaneously preserve such features (i.e. circular limit cycle and constant angular velocity) for the clock dynamics at each temperature. We can nevertheless approximately assume that this is the case for two temperatures (Fig. 16), and this assumption is supported by the fact that our model explained the phase resetting by two-temperature signals (i.e. composed of 25°C and 30°C, 35°C, or 37.5°C respectively). It is uncertain, however, whether this assumption holds for any arbitrary number of temperatures. To test this assumption, we need to scan the responses to shifts between different combinations of before-and after-shift temperatures (e.g. by varying each from 22.5°C to 37.5°C with a 2.5°C step), and examine whether we can assume the above feature for each involved temperature, and then, by tuning the relative geometry among their circular limit cycles (i.e. $LC_{22.5°C}$, $LC_{25°C}$, … $LC_{37.5°C}$), coherently recapitulate the steady-state responses to all scanned temperature shifts. If so, this approach can efficiently reveal the effects of temperature continuously across a wide range (i.e. 22.5°C to 37.5°C) and guide further mechanistic studies.

To further simplify our model in simulating the phase resetting by 25°C pulses, on top of the above assumption (i.e. circular limit cycle and constant angular velocity), we assumed a constant radial relaxation timescale, and used the simple *Poincaré* oscillator equations to incorporate these stringent assumptions. The *Poincaré* oscillator captures the cyanobacterial clock in relating its stochastic phasing to an unstable singularity. Although it does not affect this major inference, the fact that our systematically fitted model (with only six free parameters – $\frac{R_{25°C}}{d_{25°C,35°C}}$, $\frac{R_{35°C}}{d_{25°C,35°C}}$, $\alpha_{25°C-35°C}$, $\alpha_{35°C-25°C}$, k, ε) is unable to accurately reproduce some quantitative features in the data (e.g. the discrepancies between computed and measured PTCs of 9 h, 12 h, and 15 h 25°C pulses in Fig. 20) indicates that the *Poincaré* oscillator over-simplifies the cyanobacterial clock to some extent. Nevertheless, the simplicity of its mathematical descriptions is clearly advantageous in permitting convenient and intuitive analysis of the data.

3.4 Data and software availability

Raw microscopy data and codes for microscopy data analysis are accessible at Dataset: https://www.dropbox.com/sh/3ibv70v5myx2nfg/AAA6sv2ZS8eOzwJqX5MOwuNXa?dl=0.

Setup of automatic entrainment device, dataset of extracted phase resetting responses, codes for model fitting and simulations, and western blot gel images are accessible at Dataset: http://dx.doi.org/10.17632/4pwgckvgjc.1.

3.5 Additional resources

Step motor tutorial: https://www.norwegiancreations.com/2014/12/arduino-tutorial-stepper-motor-with-easydriver/

Chapter 4

Discussion

For decades, it has been known that circadian systems exhibit resetting-stimuli-induced attenuation of oscillations (Engelmann et al., 1978; Grone et al., 2011; Huang et al., 2006; Johnson and Kondo, 1992; Malinowski et al., 1985; Peterson, 1980a; Saunders, 1978; Taylor et al., 1982; Winfree, 1970, 2010). However, the single-cell behavior (arrhythmicity vs. desynchronization, Fig. 2) underlying this phenomenon has remained obscure due to the experimental difficulty of perturbing and monitoring cellular clocks in many organisms. Here we explored the mechanistic basis of resetting-stimuli-induced attenuation of oscillations in the unicellular cyanobacterium *S.elongatus*. By scanning its responses to temperature changes, we found that population-level damping of oscillations occurs because critical perturbations elicit stochastic phases of oscillations (i.e. desynchronization) in individual cells. With an experimentally constrained model, we explained the measured phase shifts by the structure of the clock as an oscillatory dynamical system, and related the induction of stochastic phases to one unstable singularity inside the stable limit cycle characteristic of circadian oscillations.

The current imaging setup could be further improved (see Methods) to let us analyze the full relaxation processes in establishing the phase shifts; and using the improved imaging setup, a refined mapping around the critical perturbations would permit a close examination of the local dynamical properties around the unstable singularity. Moreover, future mechanistic investigations are needed to link the dynamical properties to the underlying clockwork, to enable insight into the molecular nature of the singularity at a certain temperature and why it is unstable in terms of

molecular composition. The general insights into individual cellular clocks can also be built upon to study multicellular circadian systems (Liu et al., 2007, 1997), and to examine how cell-to-cell communication, either local or global, regulates a system's collective susceptibility to interruption of accurately timed rhythmicity (An et al., 2013; Jewett et al., 1991; Roberts et al., 2015).

Cellular circadian clocks are molecular oscillators (Bell-Pedersen et al., 2005). The molecular players of the clock machinery vary considerably across different taxa (e.g. bacteria, algae, plants, and animals) (Bell-Pedersen et al., 2005; Paranjpe and Sharma, 2005; Rosbash, 2009; Young and Kay, 2001), but they all constitute self-sustained oscillatory systems that possess the conserved properties (e.g. circadian periodicity, entrainment) of a circadian clock. In this study, as we do not yet understand the molecular mechanisms by which temperature affects the cyanobacterial clock, we built a conceptual rather than detailed molecular model by employing limit cycle theory to describe the clock as an oscillatory system (Strogatz, 2001; Winfree, 2010). Given the disparate molecular clockwork among different organisms, such abstraction was also employed to enable broadly comparing the cellular clocks in different organisms.

Although generally falling into the category of self-sustained oscillatory systems, the cellular clocks in different organisms may have distinct dynamical structures that govern their responses to critical perturbations (desynchronization vs. arrhythmicity) and affect the clocks' functioning. Specifically, as an oscillatory system, the clock must have a singularity inside the stable limit cycle characteristic of circadian oscillations, while this singularity could be either stable or unstable (Leloup and Goldbeter, 2000; Strogatz, 2001). The cyanobacterial clock has an unstable singularity (and so might the mammalian clock (see Methods for a detailed speculation)) and resetting stimuli

that bring the clock close to the unstable singularity will induce stochastic phases (desynchronization) (Fig. 30A; black curve towards dot at the center). The singularity, however, could be stable for cellular clocks in other organisms (Fig. 30B; solid dot) (Huang et al., 2006; Leloup and Goldbeter, 2001). In this case, there must be an unstable limit cycle (dashed circle) separating the two attractors – the stable singularity and the stable limit cycle – from each other. Given this dynamical structure, if brought to the interior of the unstable limit cycle by resetting stimuli (black curve projecting into shaded yellow region), the clock will be attracted into the stable singularity and become arrhythmic. Thus, as hypothesized previously (Leloup and Goldbeter, 2000), the stability of the singularity can explain the clock's response to critical perturbations; clocks with a stable singularity will exhibit arrhythmicity, whereas those with an unstable singularity will exhibit desynchronization among individual cells. Moreover, the resetting stimuli resulting in arrhythmicity in the case of a stable singularity are much more abundant than those that elicit desynchronization with an unstable singularity (Fig. 30, comparing (B) entire shaded region vs. (A) proximity of small dot at the center). Given that the existence of a singularity is intrinsic to the clock as an oscillator, although both types of behavior are unavoidable interruptions to accurately-timed circadian rhythmicity, desynchronization in the case of an unstable singularity is far less likely to occur. Thus, in this regard, a cellular clock with an unstable singularity (e.g. the cyanobacterial clock) is more robust than one with a stable singularity (and an unstable limit cycle).

Oscillations in general are a prevalent and significant phenomenon in biology (Kruse and Jülicher, 2005). They are hard to interpret, however, because oscillations arise from a nonlinear system of interacting components, and the observable dynamical features of an oscillator (e.g. period,

amplitude, robustness) are not intuitively linked to the properties of its individual components (Friesen and Block, 1984). The systematic approach reflected in our work will be useful in organizing the rapidly growing mechanistic knowledge of various oscillatory systems, and suggesting future experiments and directions to address.

References

An, S., Harang, R., Meeker, K., Granados-Fuentes, D., Tsai, C.A., Mazuski, C., Kim, J., Doyle, F.J., Petzold, L.R., and Herzog, E.D. (2013). A neuropeptide speeds circadian entrainment by reducing intercellular synchrony. Proc. Natl. Acad. Sci. U. S. A. *110*, E4355–E4361.

Bell-Pedersen, D., Cassone, V.M., Earnest, D.J., Golden, S.S., Hardin, P.E., Thomas, T.L., and Zoran, M.J. (2005). Circadian rhythms from multiple oscillators: lessons from diverse organisms. Nat. Rev. Genet. *6*, 544–556.

Beuter, A., Glass, L., Mackey, M.C., and Titcombe, M.S. (2003). Nonlinear Dynamics in Physiology and Medicine (Springer Science & Business Media).

Chabot, J.R., Pedraza, J.M., Luitel, P., and van Oudenaarden, A. (2007). Stochastic gene expression out-of-steady-state in the cyanobacterial circadian clock. Nature *450*, 1249–1252.

Deng, Z., Arsenault, S., Caranica, C., Griffith, J., Zhu, T., Al-Omari, A., Schüttler, H.-B., Arnold, J., and Mao, L. (2016). Synchronizing stochastic circadian oscillators in single cells of Neurospora crassa. Sci. Rep. *6*, 35828.

Dunlap, J.C., Loros, J.J., and DeCoursey, P.J. (2009). Chronobiology: Biological Timekeeping (Sinauer Associates, Inc.).

Engelmann, W., Johnsson, A., Karlsson, H.., Fernald, R., and Schimmel, M.-L. (1978). Attenuation of the petal movement rhythm in Kalanchoe with light pulses [circadian rhythm, phase shift, point of singularity, arrhythmicity, ornamental plant]. Physiol. Plant.

Friesen, W.O., and Block, G.D. (1984). What is a biological oscillator? Am. J. Physiol. *246*, R847-853.

Gooch, V. (2007). Limit Cycle Displacement Model of Circadian Rhythms. Fac. Work. Pap.

Grone, B.P., Chang, D., Bourgin, P., Cao, V., Fernald, R.D., Heller, H.C., and Ruby, N.F. (2011). Acute light exposure suppresses circadian rhythms in clock gene expression. J. Biol. Rhythms *26*, 78–81.

Gutu, A., and O'Shea, E.K. (2013). Two antagonistic clock-regulated histidine kinases time the activation of circadian gene expression. Mol. Cell *50*, 288–294.

Hosokawa, N., Kushige, H., and Iwasaki, H. (2013). Attenuation of the posttranslational oscillator via transcription–translation feedback enhances circadian-phase shifts in Synechococcus. Proc. Natl. Acad. Sci. U. S. A. *110*, 14486–14491.

Huang, G., Wang, L., and Liu, Y. (2006). Molecular mechanism of suppression of circadian rhythms by a critical stimulus. EMBO J. *25*, 5349–5357.

Hubbard, J.H., and West, B.H. (1995). Differential Equations: A Dynamical Systems Approach: A Dynamical Systems Approach. Part II: Higher Dimensional Systems (Springer Science & Business Media).

Ito, H., Mutsuda, M., Murayama, Y., Tomita, J., Hosokawa, N., Terauchi, K., Sugita, C., Sugita, M., Kondo, T., and Iwasaki, H. (2009). Cyanobacterial daily life with Kai-based circadian and diurnal genome-wide transcriptional control in Synechococcus elongatus. Proc. Natl. Acad. Sci. *106*, 14168–14173.

Jewett, M.E., Kronauer, R.E., and Czeisler, C.A. (1991). Light-induced suppression of endogenous circadian amplitude in humans. Nature *350*, 59–62.

Jewett, M.E., Forger, D.B., and Kronauer, R.E. (1999). Revised limit cycle oscillator model of human circadian pacemaker. J. Biol. Rhythms *14*, 493–499.

Johnson, C.H. (1999). Forty years of PRCs: What have we learned? Chronobiol. Int. *16*, 711–743.

Johnson, C.H., and Kondo, T. (1992). Light pulses induce “singular” behavior and shorten the period of the circadian phototaxis rhythm in the CW15 strain of Chlamydomonas. J. Biol. Rhythms *7*, 313–327.

Kondo, T., Strayer, C.A., Kulkarni, R.D., Taylor, W., Ishiura, M., Golden, S.S., and Johnson, C.H. (1993). Circadian rhythms in prokaryotes: luciferase as a reporter of circadian gene expression in cyanobacteria. Proc. Natl. Acad. Sci. U. S. A. *90*, 5672–5676.

Kruse, K., and Jülicher, F. (2005). Oscillations in cell biology. Curr. Opin. Cell Biol. *17*, 20–26.

Leloup, J.-C., and Goldbeter, A. (2000). Modeling the molecular regulatory mechanism of circadian rhythms in Drosophila. BioEssays *22*, 84–93.

Leloup, J.-C., and Goldbeter, A. (2001). A molecular explanation for the long-term suppression of circadian rhythms by a single light pulse. Am. J. Physiol. - Regul. Integr. Comp. Physiol. *280*, R1206–R1212.

Liu, A.C., Welsh, D.K., Ko, C.H., Tran, H.G., Zhang, E.E., Priest, A.A., Buhr, E.D., Singer, O., Meeker, K., Verma, I.M., et al. (2007). Intercellular Coupling Confers Robustness against Mutations in the SCN Circadian Clock Network. Cell *129*, 605–616.

Liu, C., Weaver, D.R., Strogatz, S.H., and Reppert, S.M. (1997). Cellular Construction of a Circadian Clock: Period Determination in the Suprachiasmatic Nuclei. Cell *91*, 855–860.

Malinowski, J.R., Laval-Martin, D.L., and Edmunds, L.N. (1985). Circadian oscillators, cell cycles, and singularities: light perturbations of the free-running rhythm of cell division in Euglena. J. Comp. Physiol. [B] *155*, 257–267.

Markson, J.S., Piechura, J.R., Puszynska, A.M., and O’Shea, E.K. (2013). Circadian control of global gene expression by the cyanobacterial master regulator RpaA. Cell *155*, 1396–1408.

Meerwijk, W.P.V., deBruin, G., Ginneken, C.G.V., VanHartevelt, J., Jongsma, H.J., Kruyt, E.W., Scott, S.S., and Ypey, D.L. (1984). Phase resetting properties of cardiac pacemaker cells. J. Gen. Physiol. *83*, 613–629.

Mihalcescu, I., Hsing, W., and Leibler, S. (2004). Resilient circadian oscillator revealed in individual cyanobacteria. Nature *430*, 81–85.

Nagoshi, E., Saini, C., Bauer, C., Laroche, T., Naef, F., and Schibler, U. (2004). Circadian Gene Expression in Individual Fibroblasts: Cell-Autonomous and Self-Sustained Oscillators Pass Time to Daughter Cells. Cell *119*, 693–705.

Nishiwaki, T., Satomi, Y., Nakajima, M., Lee, C., Kiyohara, R., Kageyama, H., Kitayama, Y., Temamoto, M., Yamaguchi, A., Hijikata, A., et al. (2004). Role of KaiC phosphorylation in the circadian clock system of Synechococcus elongatus PCC 7942. Proc. Natl. Acad. Sci. U. S. A. *101*, 13927–13932.

Nishiwaki, T., Satomi, Y., Kitayama, Y., Terauchi, K., Kiyohara, R., Takao, T., and Kondo, T. (2007). A sequential program of dual phosphorylation of KaiC as a basis for circadian rhythm in cyanobacteria. EMBO J. *26*, 4029–4037.

Paranjpe, D., and Sharma, V. (2005). Evolution of temporal order in living organisms. J. Circadian Rhythms *3*.

Paydarfar, D., Eldridge, F.L., and Kiley, J.P. (1986). Resetting of mammalian respiratory rhythm: existence of a phase singularity. Am. J. Physiol. *250*, R721-727.

Peterson, E.L. (1980a). Phase-resetting a mosquito circadian oscillator. J. Comp. Physiol. *138*, 201–211.

Peterson, E.L. (1980b). A limit cycle interpretation of a mosquito circadian oscillator. J. Theor. Biol. *84*, 281–310.

Plautz, J.D., Kaneko, M., Hall, J.C., and Kay, S.A. (1997). Independent Photoreceptive Circadian Clocks Throughout Drosophila. Science *278*, 1632–1635.

Pulivarthy, S.R., Tanaka, N., Welsh, D.K., Haro, L.D., Verma, I.M., and Panda, S. (2007). Reciprocity between phase shifts and amplitude changes in the mammalian circadian clock. Proc. Natl. Acad. Sci. *104*, 20356–20361.

Qin, X., Byrne, M., Xu, Y., Mori, T., and Johnson, C.H. (2010). Coupling of a Core Post-Translational Pacemaker to a Slave Transcription/Translation Feedback Loop in a Circadian System. PLOS Biol. *8*, e1000394.

Refinetti, R., Lissen, G.C., and Halberg, F. (2007). Procedures for numerical analysis of circadian rhythms. Biol. Rhythm Res. *38*, 275–325.

Roberts, L., Leise, T.L., Noguchi, T., Galschiodt, A.M., Houl, J.H., Welsh, D.K., and Holmes, T.C. (2015). Light Evokes Rapid Circadian Network Oscillator Desynchrony Followed by Gradual Phase Retuning of Synchrony. Curr. Biol. *25*, 858–867.

Rosbash, M. (2009). The Implications of Multiple Circadian Clock Origins. PLOS Biol. *7*, e1000062.

Rust, M.J., Markson, J.S., Lane, W.S., Fisher, D.S., and O'Shea, E.K. (2007). Ordered phosphorylation governs oscillation of a three-protein circadian clock. Science *318*, 809–812.

Rust, M.J., Golden, S.S., and O'Shea, E.K. (2011). Light-Driven Changes in Energy Metabolism Directly Entrain the Cyanobacterial Circadian Oscillator. Science *331*, 220–223.

Saunders, D.S. (1978). An experimental and theoretical analysis of photoperiodic induction in the flesh-Fly,Sarcophaga argyrostoma. J. Comp. Physiol. *124*, 75–95.

Strogatz, S.H. (2001). Nonlinear Dynamics And Chaos: With Applications To Physics, Biology, Chemistry, And Engineering (Cambridge, MA: Westview Press).

Sun, M., Wang, Y., Xu, X., and Yang, L. (2016). Dynamical mechanism of circadian singularity behavior in Neurospora. Phys. Stat. Mech. Its Appl. *457*, 101–108.

Takai, N., Nakajima, M., Oyama, T., Kito, R., Sugita, C., Sugita, M., Kondo, T., and Iwasaki, H. (2006). A KaiC-associating SasA-RpaA two-component regulatory system as a major circadian timing mediator in cyanobacteria. Proc. Natl. Acad. Sci. U. S. A. *103*, 12109–12114.

Taniguchi, Y., Takai, N., Katayama, M., Kondo, T., and Oyama, T. (2010). Three major output pathways from the KaiABC-based oscillator cooperate to generate robust circadian kaiBC expression in cyanobacteria. Proc. Natl. Acad. Sci. U. S. A. *107*, 3263–3268.

Taylor, W., Krasnow, R., Dunlap, J.C., Broda, H., and Hastings, J.W. (1982). Critical pulses of anisomycin drive the circadian oscillator inGonyaulax towards its singularity. J. Comp. Physiol. *148*, 11–25.

Teng, S.-W., Mukherji, S., Moffitt, J.R., de Buyl, S., and O'Shea, E.K. (2013). Robust circadian oscillations in growing cyanobacteria require transcriptional feedback. Science *340*, 737–740.

Ukai, H., Kobayashi, T.J., Nagano, M., Masumoto, K., Sujino, M., Kondo, T., Yagita, K., Shigeyoshi, Y., and Ueda, H.R. (2007). Melanopsin-dependent photo-perturbation reveals desynchronization underlying the singularity of mammalian circadian clocks. Nat. Cell Biol. *9*, 1327–1334.

Waller, L., Tian, L., and Barbastathis, G. (2010). Transport of Intensity phase-amplitude imaging with higher order intensity derivatives. Opt. Express *18*, 12552–12561.

Winfree, A.T. (1970). Integrated view of resetting a circadian clock. J. Theor. Biol. *28*, 327–374.

Winfree, A.T. (2010). The Geometry of Biological Time (New York; London: Springer).

Xu, Y., Ma, P., Shah, P., Rokas, A., Liu, Y., and Johnson, C.H. (2013). Non-optimal codon usage is a mechanism to achieve circadian clock conditionality. Nature *495*, 116–120.

Yakir, E., Hassidim, M., Melamed-Book, N., Hilman, D., Kron, I., and Green, R.M. (2011). Cell autonomous and cell-type specific circadian rhythms in Arabidopsis. Plant J. *68*, 520–531.

Yang, Q., Pando, B.F., Dong, G., Golden, S.S., and van Oudenaarden, A. (2010). Circadian gating of the cell cycle revealed in single cyanobacterial cells. Science *327*, 1522–1526.

Young, M.W., and Kay, S.A. (2001). Time zones: a comparative genetics of circadian clocks. Nat. Rev. Genet. *2*, 702–715.